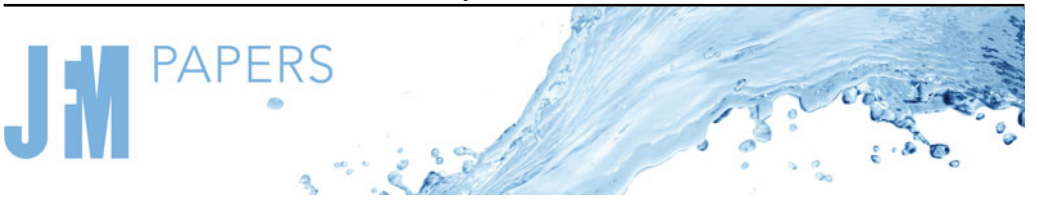
J. Fluid Mech. (2026), *vol.* 1041, A19, doi:10.1017/jfm.2026.11854



Transition of swept-wing boundary-layer flow induced by a forward-facing step

Jordi Casacuberta[1], **Koen J. Groot**[2], **Stefan Hickel**[1] **and Marios Kotsonis**[1]

[1]Department of Flow Physics and Technology, Faculty of Aerospace Engineering, Delft University of Technology, Kluyverweg 1, Delft 2629HS, The Netherlands

[2]Department of Mechanical Engineering, University of Wyoming, Laramie, WY 82071, USA

Corresponding author: Jordi Casacuberta, j.casacubertapuig@tudelft.nl

(Received 14 September 2025 UTC; revised 31 May 2026 UTC; accepted 14 June 2026 UTC)

This work investigates the laminar–turbulent transition of an incompressible swept-wing boundary-layer flow interacting with a forward-facing step using direct numerical simulations and two-dimensional linear secondary stability analysis. The focus is placed on the most critical transition scenario, where the step abruptly shifts the transition front upstream. A single-wavelength stationary crossflow perturbation is artificially triggered and allowed to develop upstream of the step. The effect of the amplitude of the incoming perturbation on the salient mechanisms of instability at the step are assessed for a fixed step height. The regime of abrupt laminar–turbulent transition at the step develops only in the case of the largest incoming perturbation amplitude considered, implying that the transition regime due to the step cannot be categorised exclusively based on local Reynolds number and instability wavelength. Step-induced transition is attributed to the stationary deformation of the shear layer immediately downstream of the step, thereby promoting rapid spatial amplification of high-frequency unsteady instabilities. The mechanisms supporting this shear-layer deformation, a mixture of linear and nonlinear growth effects, are examined by deriving energy-balance equations for the stationary spanwise-harmonic perturbation modes.

Key words: boundary layer stability, aerodynamics

1. Introduction

Achieving and maintaining laminar flow on large swept surfaces of transport aircraft poses a considerable challenge for aerodynamic design. Surface roughness, for instance, contamination by insects and other debris, rivets or joints introducing sharp surface

© The Author(s), 2026. Published by Cambridge University Press. This is an Open Access article, distributed under the terms of the Creative Commons Attribution licence (https://creativecommons.org/licenses/by/4.0/), which permits unrestricted re-use, distribution and reproduction, provided the original article is properly cited.

https://doi.org/10.1017/jfm.2026.11854 Published online by Cambridge University Press

features, is a source of significant laminar flow deterioration. However, the boundary layer of aircraft-wing flow ought to remain laminar over the largest possible extent to reduce the viscous drag and, hence, the fuel consumption of the aircraft. To guide manufacturing tolerances for laminar wings and to develop transition-prediction methodologies, it is imperative to understand the influence of such surface features on flow instabilities and laminar breakdown.

Recent investigations on the topic (Tufts *et al.* 2017; Eppink 2020; Rius-Vidales & Kotsonis 2020, 2021, 2022) focused on effects of two-dimensional (i.e. invariant in one spatial direction) forward-facing steps on transition driven by the spatial amplification of the stationary crossflow instability (CFI). In this context, the literature distinguishes three transition regimes induced by a forward-facing step, according to the upstream shift of the transition front: a negligible shift, a notable shift and an abrupt shift to a location immediately downstream of the step. The present work investigates theoretically and numerically the third regime, in which the step produces an abrupt upstream shift of the transition front. To this end, the pertinent flow structures are examined.

1.1. *The CFI*

Stability analysis of boundary-layer flow typically deals with the evolution of initially small-amplitude perturbations on a reference laminar flow state, the so-called unperturbed base flow (Mack 1984; Arnal 1993; Schmid & Henningson 2001; Theofilis 2003). In this work the base flow is the three-dimensional boundary layer over a swept wing. Laminar–turbulent transition is initiated by the exponential amplification of a primary stationary crossflow perturbation; this is the prevalent scenario in swept-wing flow subject to a low-disturbance environment as in free flight (Saric *et al.* 2003). Deyhle & Bippes (1996) discuss the receptivity conditions leading to dominance of the stationary (i.e. zero temporal frequency) or the travelling (i.e. non-zero temporal frequency) form of the CFI. The growth of a stationary CFI in the leading-edge-orthogonal (or chordwise) direction results in the amplification of so-called co-rotating stationary crossflow vortices. The axes of the crossflow vortices are approximately aligned with the direction of the streamlines in the outer-flow region (Bippes 1999; Haynes & Reed 2000).

The stationary vortical action of the CFI is responsible for the strong modulation of the boundary layer and consequent appearance of vigorous shear layers. These, in turn, give rise and sustain secondary instabilities, typically harbingers of laminar breakdown. Secondary instabilities are mainly classified based on their frequency content and location around the crossflow vortex as type I (or z mode), type II (or y mode) (Malik *et al.* 1999) and type III (Fischer & Dallmann 1991; Koch *et al.* 2000). For further details on the behaviour of a secondary CFI, the reader is referred to the numerical work of, e.g. Högberg & Henningson (1998), Wassermann & Kloker (2002) and Li *et al.* (2016*b*), the experimental work of, e.g. White & Saric (2005) and Serpieri & Kotsonis (2016), and work on stability analysis of, e.g. Bonfigli & Kloker (2007) and Groot *et al.* (2018).

In recent years, an increasing number of studies have performed stability analyses of the secondary CFI using a non-orthogonal coordinate system (Li & Choudhari 2011; Casacuberta *et al.* 2022*a*; Ambrosino *et al.* 2025; Groot *et al.* 2025). In this formulation, the spanwise axis is aligned with the wing's leading edge, while the streamwise axis follows the direction of the stationary crossflow vortex. This choice both enforces spanwise periodicity and naturally incorporates the assumption of slow flow variation along the crossflow-vortex direction.

https://doi.org/10.1017/jfm.2026.11854 Published online by Cambridge University Press

1.2. *Alternative routes to transition beyond modal instability*

Morkovin (1969) introduced the notion that a primary instability mechanism, such as a CFI, can be bypassed by 'another strongly amplifying mechanism'. Throughout the years, the idea of a bypass transition has been subject to debate, especially under the influence of surface features. Nonetheless, the existence of alternative routes towards transition is presently well established (Reshotko 2001).

Ellingsen & Palm (1975) demonstrate that for an initial three-dimensional perturbation in an inviscid shear layer (i.e. neglecting the viscous term in the perturbation equation) its streamwise component may grow linearly (or algebraically, as opposed to exponentially) in time by generating streaks, namely, alternating regions of high- and low-speed fluid. Landahl (1975, 1980) further elaborated on the linear mechanism producing the streaks, a process now commonly referred to as the lift-up effect. Algebraic perturbation growth has been ascribed mathematically to the non-normality of the linear operator governing the evolution of perturbations, i.e. the non-orthogonality of its associated eigenfunctions (Butler & Farrell 1992; Trefethen *et al.* 1993; Reddy & Henningson 1993; Schmid & Henningson 2001).

Similar to the classic stationary CFI, sufficiently amplified streaky structures can sustain secondary instabilities (Andersson *et al.* 2001; Asai *et al.* 2002; Brandt *et al.* 2003; Konishi & Asai 2004; Brandt 2007; Ricco *et al.* 2011), eventually leading to premature breakdown and transition, even if the streaks are predicted to decay asymptotically. This scenario typically arises in the wake of a critical three-dimensional surface feature in unswept conditions (De Tullio *et al.* 2013; Loiseau *et al.* 2014; Casacuberta *et al.* 2020). It may also occur during what is most commonly understood as bypass transition, where so-called Klebanoff modes (Kendall 1985) develop in two-dimensional flow subjected to moderate-to-high levels of free-stream turbulence (Klebanoff 1971; Westin *et al.* 1994; Matsubara & Alfredsson 2001; Jacobs & Durbin 2001; Brandt *et al.* 2004; Zaki & Durbin 2005). Analogous to the instability mechanisms associated to Görtler vortices (Swearingen & Blackwelder 1987), secondary instabilities of streaks are typically classified as either symmetrical (called varicose) or anti-symmetrical (called sinuous) based on their eigenmode shape relative to the streak shape. The spatial growth of sinuous and varicose instabilities leads to the shedding of quasi-streamwise-oriented vortices and hairpin-like vortices, respectively (Asai *et al.* 2002; Brandt & Henningson 2002; Konishi & Asai 2004).

Velocity streaks have been observed close downstream of a forward-facing step under both unswept (Stüer *et al.* 1999; Wilhelm *et al.* 2003; Marino & Luchini 2009; Lanzerstorfer & Kuhlmann 2012) and swept (Casacuberta *et al.* 2025) conditions and their origin has been attributed to the lift-up effect (Lanzerstorfer & Kuhlmann 2012; Casacuberta *et al.* 2025). The potential impact of such streaks on the mechanisms of transition advancement due to the step is at present not fully elucidated. It is presently well established that in swept-wing flow, the short-term algebraic growth of streaks can act as a precursor to the formation of crossflow vortices. Although the amplification of a CFI is primarily driven by a modal instability mechanism (see the discussion above), swept-wing flow supports significant non-modal growth of localised perturbations (Breuer & Kuraishi 1994; Corbett & Bottaro 2001; Tempelmann *et al.* 2010).

1.3. *Transition advancement due to a forward-facing step*

Historically, predictions of the threshold height of a surface feature influencing transition have relied on correlation parameters. The so-called roughness Reynolds number stands out in this regard,

https://doi.org/10.1017/jfm.2026.11854 Published online by Cambridge University Press

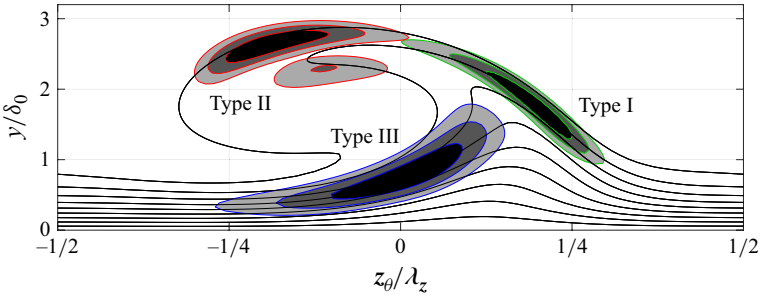


Figure 1. Sketch of classic secondary crossflow instabilities. Isocontours of stability eigenmode shapes (40 %, 60 % and 80 % of maximum value) corresponding to type I (5.2 kHz and green), II (8 kHz and red) and III (1 kHz and blue) at $x/\delta_0 = 275$ for the large-amplitude case without a step (see § 2.2) analysed in this work. Solid black lines are velocity isolines of the steady perturbed flow illustrating the stationary crossflow vortex.

$$Re_{hh} = \frac{u_h h}{\nu}, \tag{1.1}$$

where h denotes the height of the feature, ν is the kinematic viscosity and u_h expresses the velocity at the height of the surface feature in the unperturbed flow, i.e. without the surface feature; see, for instance, Smith & Clutter (1959). For surface steps, correlations between the Re_{hh} and the location of the transition front are provided by Drake *et al.* (2010) for an unswept flat plate with a prescribed favourable pressure gradient and by Duncan Jr. *et al.* (2013) for a swept flat plate. However, Re_{hh} does not serve as a universal predictive criterion and recent studies on steps have focused on elucidating the physical mechanisms governing laminar–turbulent transition.

Casacuberta *et al.* (2021, 2022*b*, 2024, 2025) examined the stationary interaction between a forward-facing step and a pre-existing CFI, segregating two distinct processes. First, the upward displacement of the CFI as it approaches the step and passes over it, as also reported experimentally (Eppink 2020; Rius-Vidales & Kotsonis 2021). Second, the rapid spatial amplification of stationary perturbation streaks near the wall, both upstream and downstream of the step. These streaks manifest as alternating high- and low-speed flow regions aligned along the step-edge (or wingspan) direction. Their structural identification aligns with previously reported instability characteristics at the step (Tufts *et al.* 2017; Eppink 2020; Rius-Vidales & Kotsonis 2021). However, their potential role in promoting transition remains unexplored.

Tufts *et al.* (2017) report the presence of a travelling mode in the region of local flow recirculation at the step, attributing the advancement of the transition front to its influence. Eppink (2020) ascribes early transition to unsteady vortex shedding emanating from the deformed shear layer at the step which, in turn, is triggered by the growth of unsteady perturbations in the shear layer past the step. The role of classic secondary crossflow instabilities in promoting transition is deemed unlikely by Eppink (2020). Rius-Vidales & Kotsonis (2022) experimentally measure significant temporal fluctuations on both the outer and inner sides of the lateral upward-inclined region of the stationary crossflow vortices past the step. These correspond respectively to the right-hand and left-hand sides in figure 1, which also highlights that the lateral upward-inclined region is dominated by the type-I instability. The scenario of abrupt transition at the step is linked to fluctuations originating from the inner side (Rius-Vidales & Kotsonis 2022).

Rius-Vidales & Kotsonis (2022) note that, while these inner unsteady fluctuations originate in the region where the type-III secondary CFI develops, their measured frequencies are significantly higher than those of the type-III instability. Simultaneously,

https://doi.org/10.1017/jfm.2026.11854 Published online by Cambridge University Press

fluctuations on the inner side do not correlate spatially with the high-frequency type-I and type-II secondary crossflow instabilities (Rius-Vidales & Kotsonis 2022). Together, these observations suggest a distinct unsteady mechanism at the step.

1.4. *Objectives and structure of the present work*

In summary, experimental evidence suggests the existence of an unexplored transition mechanism in swept-wing flow that arises from the interaction between a forward-facing step and a pre-existing stationary CFI. This mechanism potentially shifts the transition front at the step by effectively bypassing the growth of classic secondary crossflow instabilities. However, several open questions remain regarding the nature and origin of this mechanism, the potential influence of the recirculating-flow region or the steady deformation of the shear layer at the step, and the effects of the CFI amplitude.

To contribute to this discussion, direct numerical simulations (DNS) and two-dimensional linear secondary stability analysis is used here to simulate a three-dimensional incompressible swept forward-facing-step flow and examine the stationary and unsteady perturbation evolution at the step for a range of incoming CFI amplitudes. The problem set-up and methodology are described in § 2. In § 3 energy-balance equations for stationary spanwise-harmonic perturbation modes are developed. In §§ 4 and 5 the interaction between the step and the incoming CFI is examined and the energy-balance equations are evaluated. The appearance and dynamics of unsteady instabilities are analysed in § 6. Finally, the mechanisms of transition induced by the step in relation to the widely established transition paths is conceptualised in § 7.

2. Methodology

2.1. *Definition of flow problem and notation*

The flow problem (figure 2) encompasses a three-dimensional incompressible swept-wing flow modelled as flat-plate flow (i.e. the effect of wall curvature is neglected) with an imposed wing-like outer pressure evolution. The stationary crossflow perturbation is superimposed on a Falkner–Skan–Cooke similarity solution at the domain inlet. Several values of incoming crossflow-perturbation amplitude are considered. A detailed description of the set-up is provided by Casacuberta *et al.* (2022*b*), guided by the experimental work of Rius-Vidales & Kotsonis (2021) on a 45° swept wing.

The inflow free-stream chordwise velocity, u_∞, and the 99 % thickness of the inflow chordwise-velocity profile, δ_0, are chosen as characteristic quantities of the flow problem. The boundary-layer displacement thickness at the inlet is $\delta_0^\star = 0.29\delta_0$, the Reynolds number is $Re = u_\infty \delta_0/\nu = 791.37$, the spanwise free-stream velocity is $w_\infty = -1.24u_\infty$ and the CFI perturbation wavelength in the direction of wing span (z) is $\lambda_z = 9.73\delta_0$. The present choice of perturbation wavelength yields the largest amplification factor of the stationary crossflow vortices at the end of the computational domain in no-step conditions (Casacuberta *et al.* 2022*b*). Dimensional values follow the wind-tunnel experiments of Rius-Vidales & Kotsonis (2021) with $u_\infty = 15.10$ m s^{-1} and $\delta_0 = 7.71 \times 10^{-4}$ m.

The main coordinate system, $\boldsymbol{x} = [x\ y\ z]^T$, is oriented relative to the wing. The x and z directions are respectively aligned with the chordwise (i.e. leading-edge-orthogonal) and spanwise (i.e. leading-edge-parallel) directions. The coordinate y indicates the wall-normal direction. The width of the computational domain is set equal to λ_z and periodic boundary conditions are applied at the transverse boundaries. The vector of state variables is denoted by $\boldsymbol{q} = [u\ v\ w\ p]^T = [\boldsymbol{v}\ p]^T$, with u, v and w indicating the velocity components in the chordwise, wall-normal and spanwise directions, respectively, and p is the static

https://doi.org/10.1017/jfm.2026.11854 Published online by Cambridge University Press

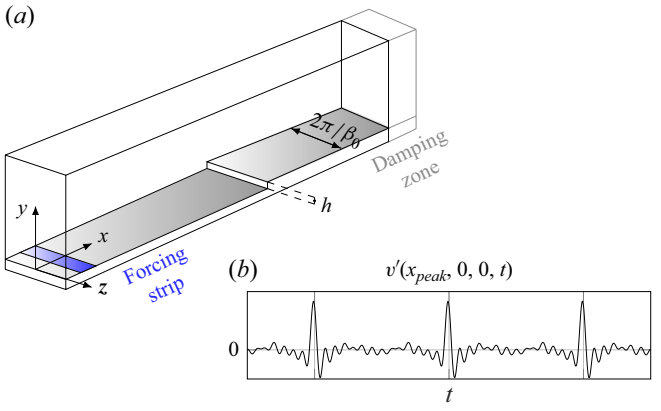


Figure 2. Sketch of the flow problem and the computational domain in (*a*) where the blue area represents the forcing strip at the wall used to excite unsteady perturbation modes. Panel (*b*) displays the signal modulating the wall-normal velocity over time at the forcing strip, with x_{peak} denoting the centre of the strip in the chordwise direction.

pressure. The effect of the wing sweep angle is incorporated in the model of flat-plate flow by expressing the free-stream velocity at the inlet into components orthogonal (u_∞) and parallel (w_∞) to the leading-edge direction.

The stability of the boundary-layer flow is typically assessed by decomposing the flow field $\boldsymbol{q}$ into a steady-state unperturbed base flow, $\boldsymbol{q}_B = [\boldsymbol{v}_B\ p_B]^T$, and a perturbation field, $\boldsymbol{q}' = [\boldsymbol{v}'\ p']^T$, such that

$$\boldsymbol{q}(x, y, z, t) = \boldsymbol{q}_B(x, y) + \boldsymbol{q}'(x, y, z, t). \tag{2.1}$$

The unperturbed base state of the swept-wing flow is inherently invariant in the spanwise direction, i.e. $\partial \boldsymbol{q}_B/\partial z = 0$, under the assumption of infinite-span wings. In the numerical procedure of this work, $\boldsymbol{q}_B$ is first computed independently. It forms the initial condition to subsequently compute the so-called steady perturbed flow, namely the superposition of the unperturbed base flow and the steady content of the perturbation field:

$$\boldsymbol{q}_{DB} = \boldsymbol{q}_B + \boldsymbol{q}', \quad \text{subject to } \partial \boldsymbol{q}'/\partial t = 0. \tag{2.2}$$

The flow field $\boldsymbol{q}_{DB}$ is numerically obtained as a steady-state solution to the Navier–Stokes equations when the inflow boundary layer is perturbed with a stationary crossflow eigenmode, to which a finite amplitude is assigned. The reader is referred to § 2.2 for details on the latter. In (2.2) the subscript DB stands for deformed base flow and denotes the steady perturbed flow. Upon subtraction of pre-computed $\boldsymbol{q}_B$ on $\boldsymbol{q}_{DB}$, the stationary perturbation field is recovered.

The unsteady flow field, $\boldsymbol{q}$, is numerically computed as the instantaneous solution to the Navier–Stokes equations when the isolated form of $\boldsymbol{q}_{DB}$ is continuously forced at selected temporal frequencies (see § 2.3 for details). For the analysis, the velocity-perturbation field is then decomposed into Fourier modes, i.e.

$$\boldsymbol{v}' = \sum_{k=-M}^{M} \sum_{j=-N}^{N} \underbrace{\tilde{\boldsymbol{v}}_{(k,j)}(x, y)\, \mathrm{e}^{\mathrm{i}(j\beta_0 z - k\omega_0 t)}}_{\boldsymbol{v}'_{(k,j)}}, \tag{2.3}$$

https://doi.org/10.1017/jfm.2026.11854 Published online by Cambridge University Press

where $\tilde{\boldsymbol{v}}_{(k,j)} = [\tilde{u}_{(k,j)}\ \tilde{v}_{(k,j)}\ \tilde{w}_{(k,j)}]^T \in \mathbb{C}^3$ denotes the Fourier coefficients, M and N indicate (one half of) the number of modes considered and $\mathrm{i}^2 = -1$. The moduli of the components of $\tilde{\boldsymbol{v}}_{(k,j)}$, the so-called amplitude functions, read $|\tilde{u}|_{(k,j)}$, $|\tilde{v}|_{(k,j)}$ and $|\tilde{w}|_{(k,j)}$.

The parameter $\beta_0 = 2\pi/\lambda_z$ in (2.3) indicates the fundamental spanwise wavenumber of the Fourier decomposition and $\omega_0 = 2\pi f_0$ indicates the fundamental angular frequency. It is noted that $\boldsymbol{v}'_{(0,-j)} = \boldsymbol{v}'^{\dagger}_{(0,j)}$, where $\dagger$ denotes the complex conjugate. An analogous Fourier decomposition is applied to the stationary pressure-perturbation field and $\tilde{p}_{(0,j)} \in \mathbb{C}$ indicates the Fourier coefficients. To quantify stationary perturbation amplification in x, the maximum along y of $|\tilde{u}|_{(0,j)} + |\tilde{u}^{\dagger}|_{(0,j)}$ is employed as a main metric; this amplitude definition is indicated by $A^u_{(0,j)} = A^u_{(0,j)}(x)$. It is emphasised that, by constraining the DNS domain length in z to λ_z, the analysis in this work is restricted to perturbations with $\beta \geqslant \beta_0$. However, it will be shown later that the dominant step-flow structure supporting laminar breakdown has a wavelength smaller than that of the fundamental CFI, as observed experimentally by Rius-Vidales & Kotsonis (2022).

2.2. *Definition of step geometry and amplitude of stationary crossflow vortices*

A two-dimensional forward-facing step (i.e. invariant in the z direction) protrudes from the flat plate. The height, $h = 0.97\delta_0$, and x location of the step in the flat plate, $x = 177.62\delta_0$, are fixed. The latter corresponds to 20 % of the chord of the reference wing model used in the experiments (Rius-Vidales & Kotsonis 2021) and the former represents approximately 50 % of the local boundary-layer thickness under reference conditions. To express the relative chordwise distance from the step, the coordinate $x_{st} = x - 177.62\delta_0$ is introduced. Eppink (2020) reports that the step height required to induce transition advancement depends on the amplitude of the incoming CFI. In the present work, the step height leads to an abrupt transition at the step only at the largest CFI amplitude considered.

The influence of the incoming CFI amplitude on the conditioning of transition is investigated. Three main flow cases are analysed, for which the nomenclature is defined as follows: the labels A, B, C denote increasing amplitude assigned to the stationary crossflow eigenmode prescribed at the inlet (table 1). Additionally, 's' and 'r' indicate step and reference (no-step) conditions, respectively. Under reference conditions, the perturbation behaviour is as follows: in configuration r.A (the small-amplitude case), the fundamental stationary CFI remains predominantly linear throughout most of the computational domain. This is illustrated in figure 3(a) by the almost exact match between the solution to the linear parabolised stability equations (LPSE) and the DNS. In configuration r.B (the medium-amplitude case), linear behaviour persists until approximately the virtual step location; see Casacuberta *et al.* (2022*b*, cf. figure 4). Finally, in configuration r.C (the large-amplitude case, which qualitatively reproduces the so-called supercritical transition scenario in the experiments of Rius-Vidales & Kotsonis 2021), nonlinear effects emerge upstream of the virtual step location; see figure 3(b).

2.3. *Set-up of the DNS*

The flow fields $\boldsymbol{q}_B$, $\boldsymbol{q}_{DB}$ and $\boldsymbol{q}'$ are computed numerically by performing DNS of the incompressible Navier–Stokes equations. An explicit third-order Runge–Kutta method is used to march the equations in time. The pressure Poisson equation is solved via the BiCGstab method up to an L_2-norm convergence threshold value of 10^{-7}. The flow fields $\boldsymbol{q}_B$ and $\boldsymbol{q}_{DB}$ are steady-state solutions to the Navier–Stokes equations. The selective frequency damping (SFD) method (Åkervik *et al.* 2006; Casacuberta *et al.* 2018) is employed to accelerate convergence towards a steady-state solution; the SFD is removed prior to halting the simulation so as not to obscure possible global instability behaviours.

https://doi.org/10.1017/jfm.2026.11854 Published online by Cambridge University Press

Case	$A^u_{(0,1)}/u_\infty\big\vert_{x=0}$	$A^u_{(0,1)}/u_\infty\big\vert_{x_{st}=0}$	Note
r.*A* (no step), s.*A* (step)	1×10^{-4}	3×10^{-3}	Small amplitude
r.*B* (no step), s.*B* (step)	3.5×10^{-3}	1×10^{-1}	Medium amplitude
r.*C* (no step), s.*C* (step)	2.6×10^{-2}	3×10^{-1}	Large amplitude

Table 1. Amplitude of the fundamental stationary crossflow perturbation at inflow ($x = 0$) and at the virtual step location ($x_{st} = 0$).

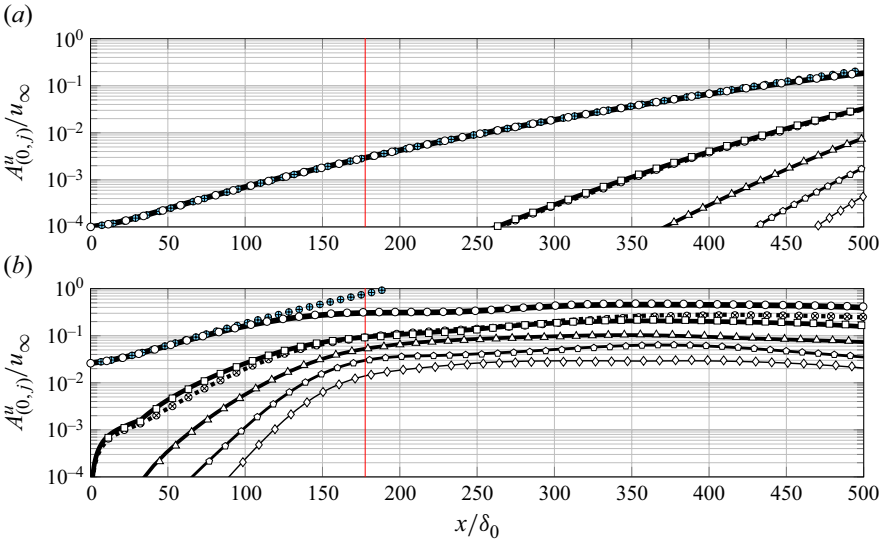


Figure 3. Chordwise evolution of the amplitude of the stationary crossflow perturbation in (*a*) the small-amplitude case, r.*A,* and (*b*) the large-amplitude case, r.*C*, without a step obtained from LPSE (blue symbols), nonlinear parabolised stability equations (white symbols) and DNS (solid lines): spanwise Fourier modes $j =$ 1–5 (thick-to-thin), $j = 0$ (dotted). The vertical red line indicates the virtual step location.

An L_2 convergence threshold of 10^{-6} is considered for all cases, except s.*C*, for which the threshold is set to 10^{-5} due to its larger computational cost. The reader is referred to Casacuberta *et al.* (2022*b*) for further details on the set-up.

The computational domain in reference conditions has dimensions $0 \leqslant x/\delta_0 \leqslant 517$, $0 \leqslant y/\delta_0 \leqslant 26$, $-4.86 \leqslant z/\delta_0 \leqslant 4.86$. In the step cases the domain length in the chordwise direction is reduced to $0 \leqslant x/\delta_0 \leqslant 245$ since the focus is placed on the mechanisms of laminar breakdown at the step. Different levels of grid density are considered for the different flow problems in this work; see table 2. The grid density in the spanwise direction for the steady perturbed flow is chosen to ensure the accurate resolution of a converged ensemble of high-order harmonic perturbation modes, as demonstrated in figure 3.

For final unsteady simulations of transitional flow, the SFD method is switched off. Moreover, the flow field is forced at selected temporal frequencies through a disturbance strip placed at the wall near the inflow (figure 2). The present forcing approach follows Wassermann & Kloker (2002). At the disturbance strip, the wall-normal velocity is

https://doi.org/10.1017/jfm.2026.11854 Published online by Cambridge University Press

		Steady ($\boldsymbol{q}_{DB}$)			Unsteady ($\boldsymbol{q}$)					
		N_x	N_y	N_z	N_x	N_y	N_z	Δx^+	Δy^+	Δz^+
Step	S.*A*	6760	504	72	—	—	—	—	—	—
	S.*B*	6760	504	72	5080 †	504	72	0.56	0.56	5.60
	S.*C*	5080 †	1008	144	5080 †	1008	144	**1.54**	**0.77**	**7.70**
No-Step	R.*A*	3380	288	72	—	—	—	—	—	—
	R.*B*	6760	576	72	5080 †	576	72	0.65	0.65	6.5
	R.*C*	6760	576	144	6760	576	144	0.67	0.67	3.35

Table 2. Grid density in the computations of steady perturbed (2.2) and unsteady (2.1) flows, where N_x, N_y and N_z respectively denote the number of grid points in the x, y and z directions. Note that in the step cases, N_y is indicative of $x_{st} \geqslant 0$. The grid spacing expressed in wall units is computed close downstream of the step x location at the z location of maximum wall shear, with bold font indicating near breakdown conditions.

† (The length of the domain in x is smaller ($245\delta_0$) than the remainder of cases ($517\delta_0$) since the analysis is restricted to near-step effects. The domain height is fixed for all cases ($26\delta_0$)).

modulated continuously in time as

$$v(x, 0, z, t) = f_s(x) \sum_{k=1}^{M_{BS}} A_k^{BS} \cos\left(\beta_0 z + 2\pi k f_0 t + \phi_k\right), \tag{2.4}$$

where t denotes time, f_0 is a fundamental temporal frequency, M_{BS} is the number of modal components, A_k^{BS} and ϕ_k respectively denote the amplitude and a random phase assigned to each modal component k and

$$f_s = \left(\frac{4\left(x - x_{BS,start}\right)\left(x_{BS,end} - x\right)}{\left(x_{BS,end} - x_{BS,start}\right)^2} \right)^3, \tag{2.5}$$

with $x_{BS,start} = 20\delta_0$ and $x_{BS,end} = 32\delta_0$ indicating the upstream and downstream limits of the disturbance strip in x. The function f_s is symmetric and has vanishing first and second derivatives at $x_{BS,start}$ and $x_{BS,end}$. A damping zone based on the SFD method is applied in the outflow region in order to suppress unwanted reflections. It is active from $x/\delta_0 \geqslant 230$ in cases s.*B,C* and from $x/\delta_0 \geqslant 475$ in cases r.*B,C*.

Presently, $f_0 = 1$ kHz, $M_{BS} = 14$, $A_{1\text{-}2}^{BS} = 0$ and $A_{3\text{-}14}^{BS} = 5 \times 10^{-3} u_\infty$ (2.4), implying that the flow field is forced at temporal frequencies ranging from 3 to 14 kHz in intervals of 1 kHz. At the start of the unsteady simulation, the forcing (2.4) is ramped up by a smooth function in time to alleviate transient effects. Based on preliminary investigations (Casacuberta *et al.* 2022*a*), lower-frequency components are not excited at the disturbance strip (although they develop further downstream), thereby preventing the strong amplification of a type-III secondary CFI upstream of the step.

The results from DNS are Fourier decomposed to recover the behaviour of steady and unsteady perturbation modes. First, the three-dimensional stationary perturbation field obtained from simulations of the steady perturbed flow (2.2) is decomposed into spanwise Fourier modes. Second, a time series of three-dimensional DNS snapshots is Fourier analysed in the spanwise direction and in time (2.3). In the reference no-step case r.*C*, 290 DNS snapshots are generated per period of the fundamental temporal frequency, i.e. $f_0 = 1$ kHz. In the step case s.*C*, at least 20 snapshots are collected per period of the critical frequency component, i.e. $f = 12$ kHz (§ 6.2).

The analysis of unsteady perturbation effects is complemented by use of pointwise temporal signals from numerical probes. An estimate of power spectral density (PSD)

https://doi.org/10.1017/jfm.2026.11854 Published online by Cambridge University Press

is computed with Welch's method of overlapped segments considering two Hamming windows with an overlap of 80 %.

2.4. *Set-up of the two-dimensional linear secondary stability analysis*

Two-dimensional linear secondary stability analysis is employed in this work to assess unsteady instability of the steady perturbed flow (2.2). A two-dimensional plane-marching stability approach is considered, popularly known as PSE-3D (Paredes 2014; Paredes *et al.* 2015), which is here formulated using a non-orthogonal coordinate system. The present method, which extends the non-orthogonal, local, two-dimensional method introduced by Li & Choudhari (2011), has gained increasing adoption in recent years for the study of instabilities of crossflow vortices and streaks in three-dimensional boundary layers (Li *et al.* 2016*a*; Wei *et al.* 2017; Choudhari *et al.* 2022; Sombaert *et al.* 2025).

The flow problem investigated requires a non-orthogonal coordinate system because the perturbation of interest is periodic in the z direction while the smallest gradients are encountered in a direction that is approximately aligned with the crossflow vortex. The latter direction, denoted x_θ, is non-orthogonal to the y–z plane; the angle between the leading-edge-orthogonal x and non-orthogonal x_θ directions will be denoted by θ.

The plane-marching stability approach is formulated on the steady perturbed flow, $\boldsymbol{q}_{DB}$ (2.2). The method imposes a slow evolution of perturbations in the x_θ direction through the ansatz

$$\boldsymbol{q}'_{BiG}(x_\theta, y, z_\theta, t) = \tilde{\boldsymbol{q}}_{BiG}(x_\theta, y, z_\theta) \exp\left[\mathrm{i}\left(\int_{x_{\theta,0}}^{x_\theta} \alpha_\theta(\bar{x}_\theta)\,\mathrm{d}\bar{x}_\theta - \omega t\right)\right] + \text{c.c.}, \tag{2.6}$$

where $\tilde{\boldsymbol{q}}_{BiG} = [\tilde{u}_{BiG}\ \tilde{v}_{BiG}\ \tilde{w}_{BiG}\ \tilde{p}_{BiG}]^T$ contains the perturbation shape functions, α_θ is the wavenumber in the x_θ direction, ω is the angular frequency (with $\omega = 2\pi f$; similar notation as in (2.3)), $x_{\theta,0}$ is the initialisation location, c.c. denotes the complex conjugate and $\bar{x}_\theta$ indicates the integration-variable equivalent of x_θ.

Substituting ansatz (2.6) into the governing (linearised) equations and dropping the second-order x_θ derivatives of $\tilde{\boldsymbol{q}}_{BiG}$ yields the plane-marching stability equations. Upon dropping the x_θ dependence of $\tilde{\boldsymbol{q}}_{BiG}$ and α_θ, the stability problem reduces to a two-dimensional (i.e. in the $z_{(\theta)}$–y plane) eigenvalue problem, that here will be referred to as the local approach. The reader is referred to Groot *et al.* (2025) for details of the non-orthogonal transformation, the full system of stability equations, the choices of boundary and auxiliary conditions, discretisation procedures and the PSE stabilisation approach (with associated length scale, $s = O(\delta_0)$; see table 4), inspired by Andersson *et al.* (1998).

Perturbation amplification is quantified with N factors, calculated as

$$N(x) = -\int_{x_0}^{x} \alpha_{\theta,i}(x_\theta(\bar{x}))\sec\theta(\bar{x})\,\mathrm{d}\bar{x} + \frac{1}{2}\ln\frac{E_{BiG}(x)}{E_{BiG}(x_0)}, \tag{2.7}$$

where

$$E_{BiG}(x) = \iint \left(|\tilde{u}_{BiG}(x_\theta(x), y, z_\theta)|^2 + |\tilde{v}_{BiG}|^2 + |\tilde{w}_{BiG}|^2\right)\mathrm{d}y\,\mathrm{d}z_\theta. \tag{2.8}$$

Here the subscript i denotes the imaginary part, $\bar{x}$ is the integration-variable equivalent of the orthogonal x coordinate and x_0 is taken to correspond to the initialisation location.

3. Energy-balance framework for stationary perturbations

The energy-balance framework for stationary spanwise-harmonic perturbations will be used to analyse the mechanisms governing stationary perturbations at the step (§ 5),

https://doi.org/10.1017/jfm.2026.11854 Published online by Cambridge University Press

responsible for modulating the shear layer in the steady perturbed flow (§ 4). The definitions introduced in this section are thus restricted to the stationary perturbation modes $\boldsymbol{v}'_{(0,j)}$ (2.3). The formulation presented here, which capitalises on the periodicity of perturbations in z, is inspired by the temporal analysis of Jin *et al.* (2021).

Let E denote the kinetic energy of stationary perturbations within a volume V, which encompasses the periodic boundaries in the z direction of length $(2\pi)/\beta_0$. It is defined via the standard Hermitian inner product of the complex-valued stationary perturbation velocity vector $\boldsymbol{v}'_{(0,j)} = [u'_{(0,j)}\ v'_{(0,j)}\ w'_{(0,j)}]^T$ with itself, i.e.

$$E = \frac{1}{2}\int_V \sum_{j=-N}^{N} \boldsymbol{v}'^{\dagger}_{(0,j)}\, \boldsymbol{v}'_{(0,j)} \mathrm{d}V = \sum_{n=0}^{N} \int_S E_{n\beta_0}\, \mathrm{d}S, \tag{3.1}$$

where S denotes the x–y cross-sectional plane of V. The modal energy density $E_{n\beta_0}$ corresponding to the wavenumber space $n\beta_0$, $n = 0, 1, \ldots, N$ is defined as

$$E_{n\beta_0} = \delta_n \frac{\pi}{\beta_0}\left(|\tilde{u}|^2_{(0,n)} + |\tilde{v}|^2_{(0,n)} + |\tilde{w}|^2_{(0,n)}\right) \qquad \begin{cases} \delta_n = 2, & n > 0, \\ \delta_n = 1, & n = 0. \end{cases} \tag{3.2}$$

This definition accounts for the conjugate symmetry of the Fourier decomposition, as the pair $\boldsymbol{v}'_{(0,n)}$ and $\boldsymbol{v}'_{(0,-n)}$ combine to yield a real-valued structure in physical space. Due to the stationary nature of perturbations, $\mathrm{d}E_{n\beta_0}/\mathrm{d}t = 0$, indicating that the mechanisms governing the evolution of $E_{n\beta_0}$ are in temporal equilibrium.

The mechanisms of energy transfer within a perturbation space $n\beta_0$ are evaluated as follows: the decomposition of stationary perturbations into spanwise modes (see (2.3) for $k = 0$) is substituted into the perturbation (A1). By factoring out the z dependence of terms, the perturbation equation can be re-expressed as

$$0 = \sum_{j=-N}^{N}\left(\mathbb{L}_{(0,j)} + \mathbb{F}^{p}_{(0,j)} - \sum_{\substack{r=-N \\ j-r\in[-N,N]}}^{N} \left(\underline{\tilde{\boldsymbol{v}}}_{(0,r)} \cdot \mathbb{B}_{(0,j-r)}\right)\right) \mathrm{e}^{ij\beta_0 z}, \tag{3.3}$$

where $\mathbb{L}_{(0,j)}(x, y) = \mathbb{A}^{I}_{(0,j)}(x, y) + \mathbb{A}^{II}_{(0,j)}(x, y) + \mathbb{F}^{v}_{(0,j)}(x, y)$ and $\mathbb{F}^{p}_{(0,j)}(x, y)$ represent the linear operators, while $\mathbb{B}_{(0,j)}(x, y)$ captures the nonlinear interactions. The underline notation ($\underline{\boldsymbol{v}}$) indicates a non-dimensional variable, referenced to δ_0 and u_∞ (§ 2.1), as the analysis is conducted using the non-dimensional form of the perturbation equation (A1). Details on the derivation and explicit analytic expressions of terms of (3.3) can be found in Appendix A.

Equation (3.3) is modally decoupled and cast into scalar energy form by taking the standard Hermitian inner product of the amplitude coefficient $\tilde{\boldsymbol{v}}_{(0,j)}$ (2.3) with the corresponding jth equation stemming from (3.3) such that

$$0 = \mathcal{P}_{n\beta_0} + \mathcal{T}_{n\beta_0} + \mathcal{D}_{n\beta_0} + \mathcal{W}_{n\beta_0} + \mathcal{N}_{n\beta_0},\ n = 0, 1, \ldots, N, \tag{3.4}$$

with

$$\mathcal{P}_{n\beta_0} = \underline{\tilde{\boldsymbol{v}}}^{\dagger}_{(0,n)}\, \mathbb{A}^{\mathrm{I}}_{(0,n)} + \mathrm{c.c.}, \quad \mathcal{T}_{n\beta_0} = \underline{\tilde{\boldsymbol{v}}}^{\dagger}_{(0,n)}\, \mathbb{A}^{\mathrm{II}}_{(0,n)} + \mathrm{c.c.}, \tag{3.5a}$$

$$\mathcal{D}_{n\beta_0} = \underline{\tilde{\boldsymbol{v}}}^{\dagger}_{(0,n)}\, \mathbb{F}^{v}_{(0,n)} + \mathrm{c.c.}, \quad \mathcal{W}_{n\beta_0} = \underline{\tilde{\boldsymbol{v}}}^{\dagger}_{(0,n)}\, \mathbb{F}^{p}_{(0,n)} + \mathrm{c.c.}, \tag{3.5b}$$

$$\mathcal{N}_{n\beta_0} = -\,\underline{\tilde{\boldsymbol{v}}}^{\dagger}_{(0,n)} \left(\sum_{\substack{r=-N \\ n-r\in[-N,N]}}^{N} \left(\underline{\tilde{\boldsymbol{v}}}_{(0,r)} \cdot \mathbb{B}_{(0,n-r)}\right)\right) + \mathrm{c.c.} \tag{3.5c}$$

https://doi.org/10.1017/jfm.2026.11854 Published online by Cambridge University Press

A factor of $(2\pi)/\beta_0$, which arises from integrating the terms in the z direction, has been omitted from the energy budget in (3.4) for simplicity.

Each term in (3.4) characterises a distinct mechanism of kinetic energy transfer within the perturbation space $n\beta_0$. The sign of each term indicates whether the corresponding mechanism acts locally in a stabilising (i.e. <0) or destabilising (i.e. >0), manner. The production term $\mathcal{P}_{n\beta_0}(x, y)$ quantifies the exchange of kinetic energy between the unperturbed base flow and the perturbations $n\beta_0$. The transport term $\mathcal{T}_{n\beta_0}(x, y)$ accounts for the advection of kinetic perturbation energy by the unperturbed base flow. The term $\mathcal{D}_{n\beta_0}(x, y)$ captures viscous effects, typically decomposed into contributions from diffusion and dissipation. Finally, $\mathcal{W}_{n\beta_0}(x, y)$ and $\mathcal{N}_{n\beta_0}(x, y)$ represent the work done by the perturbation pressure and the nonlinear interactions, respectively.

It follows from (3.3) that

$$0 = \sum_{n=0}^{N} \mathcal{P}_{n\beta_0} + \sum_{n=0}^{N} \mathcal{T}_{n\beta_0} + \sum_{n=0}^{N} \mathcal{D}_{n\beta_0} + \sum_{n=0}^{N} \mathcal{W}_{n\beta_0} + \sum_{n=0}^{N} \mathcal{N}_{n\beta_0}, \tag{3.6}$$

which is analogous to (3.4) but applies to the perturbation field as a whole.

4. Steady flow evolution

In this section, steady effects are examined. The unperturbed laminar base flow $\boldsymbol{q}_B$ (2.1) is a spatially developing three-dimensional boundary layer that deforms upon interaction with the step; see Casacuberta *et al.* (2022*b*, § 3). Specifically, the step induces regions of adverse pressure gradient both upstream and downstream of the step, together with a localised region of favourable pressure gradient around the upper step corner (Casacuberta *et al.* 2022*b*, figure 5). Flow reversal ($u_B < 0$) occurs both upstream and downstream of the step, with the shallow separation downstream of the step extending to approximately $x_{st}/\delta_0 = 2$. The unperturbed base flow is topologically identical across all cases within the 's' category (signifying step conditions; see § 2.2) and separately within the '*r*' category (signifying reference no-step conditions; see § 2.2) discussed in this work. However, the organisation of the steady perturbed flow, $\boldsymbol{q}_{DB}$, depends on the chosen amplitude of the pre-imposed stationary crossflow eigenmode.

Under reference no-step conditions, the stationary crossflow vortex is the main flow structure of the steady perturbed flow (figures 4*b* and 4*c*). As expected, in the small-amplitude case r.*A* (figure 4*a*), the structure of the steady perturbed flow remains largely similar to that of the unperturbed base flow. All planes in figure 4 are shown at $x_{st}/\delta_0 = 9.4$, a position representative of the flow organisation close downstream of the step, but downstream of the reattachment point; see figure 5 for reference. Specifically, figure 4 depicts the y–z planes of $u_{DB,s}$, the velocity component in the steady perturbed flow that points in the direction of the inviscid streamline. Additionally, black quiver arrows in figure 4 are derived from the in-plane velocity components normal to the direction of the inviscid streamline, $w_{DB,s}$, and normal to the wall, v_{DB}. Details on the computation of $u_{DB,s}$, v_{DB} and $w_{DB,s}$ can be found in Casacuberta *et al.* (2022*b*).

The step modifies the steady perturbed flow primarily through deformation of the shear layer near the wall. In case s.*C* (figure 4*f*), this deformation is significantly enhanced, compared with case s.*B* (figure 4*e*), leading to the formation of a low-momentum dip (labelled CS dip in figure 4*f*). As discussed in § 6, this CFI-step dip (abbreviated to CS dip) of low momentum, arising from the interaction between the incoming CFI and the step, plays a central role in promoting laminar breakdown. The present numerical simulations reveal that the CS dip is an inherent feature of the steady perturbed flow, with its origin

https://doi.org/10.1017/jfm.2026.11854 Published online by Cambridge University Press

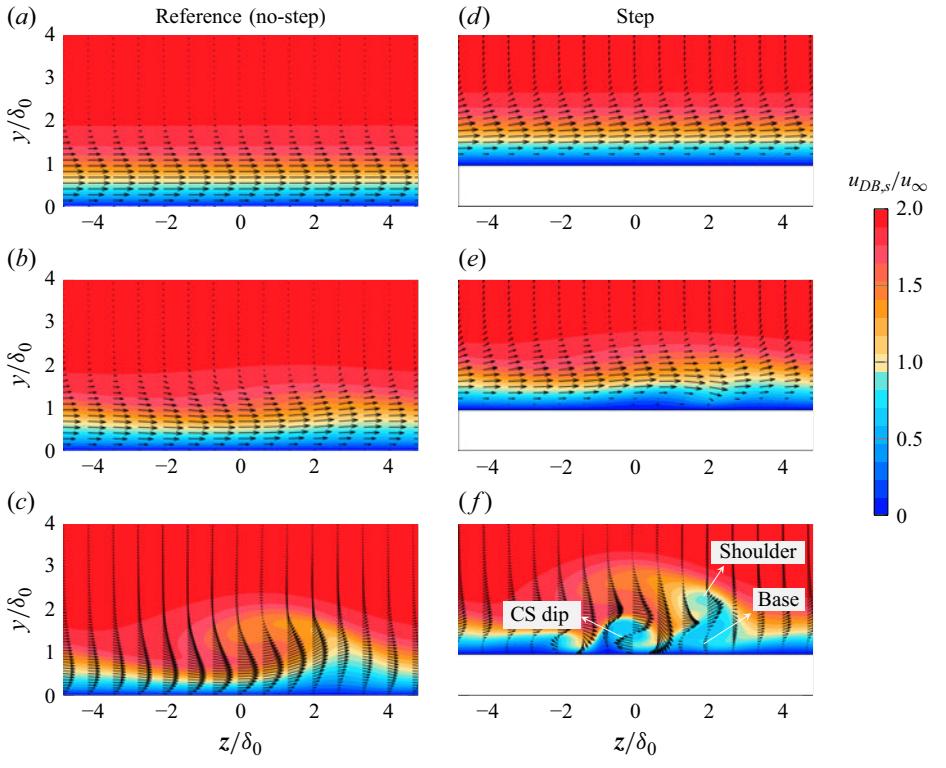


Figure 4. Topology of the steady perturbed flow illustrated by z–y planes of velocity $u_{DB,s}$ at $x_{st}/\delta_0 = 9.4$. (*a–c*) No-step cases r.*A*, r.*B*, r.*C* and (*d–f*) step cases s.*A*, s.*B*, s.*C*. The black arrows illustrate the in-plane organisation of the steady perturbed flow ($w_{DB,s}$ and v_{DB}).

examined in § 5.2. Simultaneously, the structure of the original crossflow vortex is altered by the interaction with the step. Specifically, the base, $(y, z)/\delta_0 \approx (1.5, 2)$, and part of the shoulder of the stationary crossflow vortex, $(y, z)/\delta_0 \approx (2.5, 2)$, undergo a local decrease of streamwise momentum (figure 4*f*), compared with the no-step case (figure 4*c*).

A structurally similar flow feature to the CS dip (figure 4*f*) has been observed in time-averaged experimental flows (Rius-Vidales & Kotsonis 2022). Furthermore, it is worth noting that the organisation of the steady perturbed flow downstream of the step qualitatively resembles the flow organisation described by Wassermann & Kloker (2005) in the context of a swept-wing boundary-layer subject to a pressure-gradient changeover. Wassermann & Kloker (2005) report that the reversal of the crossflow-velocity profile induces a redistribution of the spanwise shear and promotes the amplification of additional CFI modes, which may rotate in a sense opposite to the pre-existing ones.

The near-wall deformation of the shear layer past the step increases in strength with the amplitude of the incoming crossflow perturbation. This is evident in figure 4(*d–f*). To quantify this effect, the spatial distribution of the wall-shear field

$$\xi_w(x, z) = \sqrt{\left(\frac{\partial u_{DB}}{\partial y}\right)^2 + \left(\frac{\partial w_{DB}}{\partial y}\right)^2}\Bigg|_{wall} \tag{4.1}$$

is evaluated for the step cases, namely s.*A*–s.*C*, and portrayed in figure 5(*a–c*) in the range $-5 \leqslant x_{st}/\delta_0 \leqslant 25$. Additionally, figure 5(*d–f*) quantitatively characterises the x evolution

https://doi.org/10.1017/jfm.2026.11854 Published online by Cambridge University Press

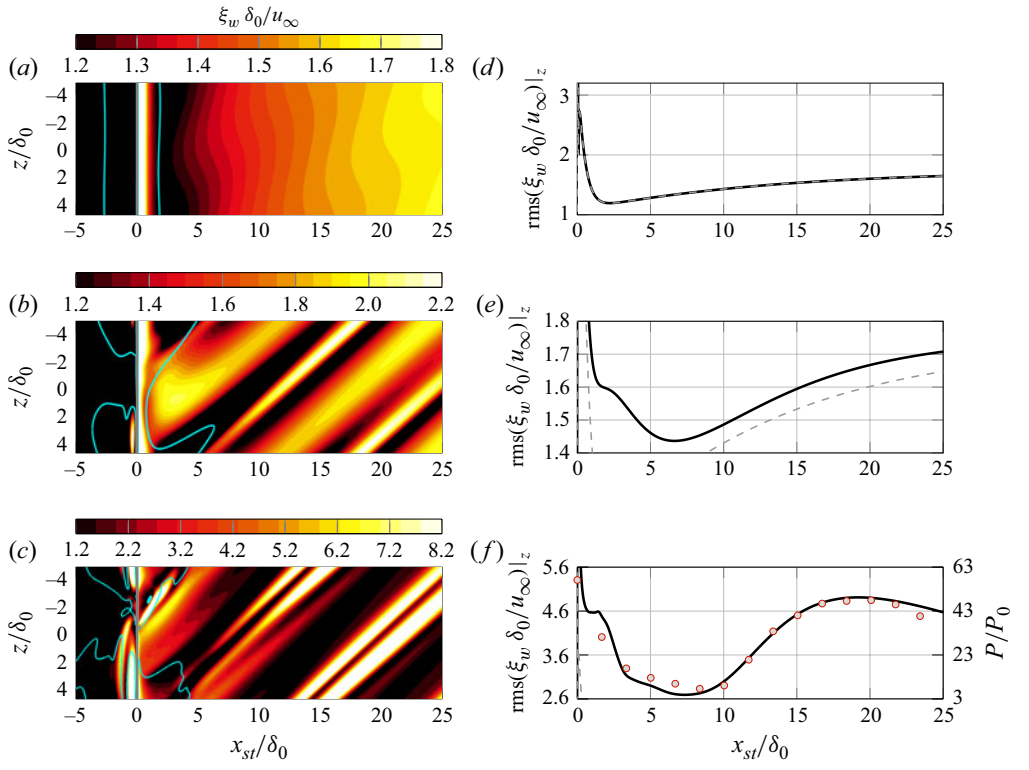


Figure 5. Wall-shear (ξ_w) contour with cyan isoline indicating $\partial u_{DB}/\partial y = 0$ at the wall (*a–c*). Evolution in x of the r.m.s. along z of wall shear (*d–f*) in cases s.*A* (*a*, *d*), s.*B* (*b*, *d*), s.*C* (*c*, *f*): steady perturbed flow from DNS (solid black line, left axis), unperturbed base flow from DNS (dashed grey line, left axis) and spatial PSD of infrared thermal measurements from Rius-Vidales & Kotsonis (2021) (red circles, right axis). The PSD P/P_0 is normalised and extracted at the fundamental CFI spanwise wavelength.

of the root mean square (r.m.s.) of ξ_w along z (solid black line), denoted by $\mathrm{rms}|_z$. For reference, the same wall-shear metric for the unperturbed base flow is included (see dashed grey line). In the small-amplitude case s.*A*, the steady perturbed flow contains regions of reverse flow both upstream and downstream of the step, as indicated by the cyan isoline marking $\partial u_{DB}/\partial y = 0$ at the wall (figure 5*a*).

In case s.*B*, the reverse-flow region extends further in x and becomes modulated at the fundamental spanwise wavelength of the incoming CFI (figure 5*b*), as also reported by Tufts *et al.* (2017). When the amplitude of the incoming CFI is further increased in case s.*C* (figure 5*c*), the reverse-flow regions fragment into individual irregular patches. Eppink (2020) also observes the emergence of isolated recirculating-flow patches for particular combinations of step height and incoming perturbation amplitude.

The red circles in figure 5*f* represent infrared thermal measurements from Rius-Vidales & Kotsonis (2021). In their experiments, the externally heated wing surface exhibits z-distributed regions of high and low temperature, corresponding to areas of weaker and stronger wall-shear stress. A spatial PSD analysis of the wall-temperature measurements is performed along the z direction. The normalised PSD extracted at the fundamental CFI spanwise wavenumber, which dominates the wall-shear evolution, serves as a key metric. This is depicted in figure 5(*f*) as red circles and denoted as P/P_0, where P_0 indicates a reference value of the PSD evolution (Rius-Vidales & Kotsonis 2021, figure 5), which has been rescaled to match the wall-shear evolution from DNS at $x_{st}/\delta_0 \approx 12$. Overall,

https://doi.org/10.1017/jfm.2026.11854 Published online by Cambridge University Press

good qualitative agreement is reported between the near-wall flow behaviour obtained from DNS (case s.C) and experiments (Rius-Vidales & Kotsonis 2021), as shown by the solid black line and red circles in figure 5(f).

5. Stationary perturbation mechanisms at the step

The mechanisms governing the steady modulation of the shear layer at the step are examined in this section. The main focus of the analysis is on the medium- (s.B) and large-amplitude (s.C) cases since the behaviour of the small-amplitude (s.A) case at the step is qualitatively similar to s.B. For reference, the key results pertaining to case s.A are presented in Appendix B.

5.1. *Evolution of stationary perturbation fields*

The evolution of stationary perturbations at the step under medium- (a,c) and large-amplitude (b,d) CFI conditions is compared in figure 6. The stationary perturbation field is decomposed into spanwise modes (§ 2): subplots (a,b) correspond to the fundamental spanwise mode, $\beta = \beta_0$, while subplots (c,d) correspond to the harmonic spanwise mode $\beta = 3\beta_0$. In the analysis of this work, the spanwise mode $\beta = 3\beta_0$ is generally indicative of (and used to illustrate) the behaviour of the higher-order spanwise modes, $\beta > \beta_0$.

The fundamental, i.e. primary-wavelength, stationary CFI gradually lifts off the surface in x and passes over the step (figures 6a and 6b). Upon interacting with the step, it produces stationary velocity-perturbation streaks of alternating sign in z just downstream of the upper step corner; their origin is attributed to linear non-modal growth driven by the lift-up effect (Casacuberta *et al.* 2025). The spanwise wavenumber of these streaks is identically $\beta = \beta_0$; they therefore appear within the fundamental spanwise perturbation mode together with the CFI (Casacuberta *et al.* 2021, 2022*b*), which develops further away from the wall. These streaks are accompanied by perturbation vortices (see also Casacuberta *et al.* 2024, 2025) whose organisation at the step is shown in figure 7 via projected streamlines and the rotated streamwise component of the perturbation vorticity,

$$\omega'_{x\sigma_B,(0,j)} = \frac{\partial w'_{\sigma_B,(0,j)}}{\partial y} - \cos(\sigma_B)\,\frac{\partial v'_{(0,j)}}{\partial z}, \tag{5.1}$$

where the streamwise-derivative contribution is neglected, $\tan(\sigma_B) = w_B/u_B$, and

$$w'_{\sigma_B,(0,j)} = w'_{(0,j)}\cos(\sigma_B) - u'_{(0,j)}\sin(\sigma_B)\,. \tag{5.2}$$

A significant difference arises in the large-amplitude case s.C: whereas in s.A and s.B the near-wall streaks rapidly decay in x (figure 6a), consistent with the trend of the accompanying perturbation vortices (figure 7), the streaks undergo a second phase of growth in x after initial decay in case s.C (figure 6b).

Near-wall perturbation streaks induced locally at the upper step corner also manifest in the high-order spanwise modes, i.e. $\beta > \beta_0$, as shown in figures 6(c) and 6(d). In case s.B, all high-order spanwise perturbation modes exhibit a qualitatively similar trend in x. In contrast, in the large-amplitude case s.C, the high-order spanwise modes display distinct growth regimes depending on the spanwise harmonic.

This distinction is quantified through the streamwise evolution of the integral perturbation kinetic energy, $\int E_{n\beta_0}\,\mathrm{d}y$, $n = 0, 1, 2, \ldots$, shown in figure 8. For reference, figures 8(a), 8(c) and 8(e) depict no-step conditions, i.e. cases *r.A*, *r.B* and *r.C*, and figure 8(b) depicts the step case s.A. Figure 8(d), illustrating case s.B, confirms that high-order spanwise perturbation modes undergo analogous growth phases, consistent with the existence of a modal inflectional instability of the step-distorted base-flow profiles

https://doi.org/10.1017/jfm.2026.11854 Published online by Cambridge University Press

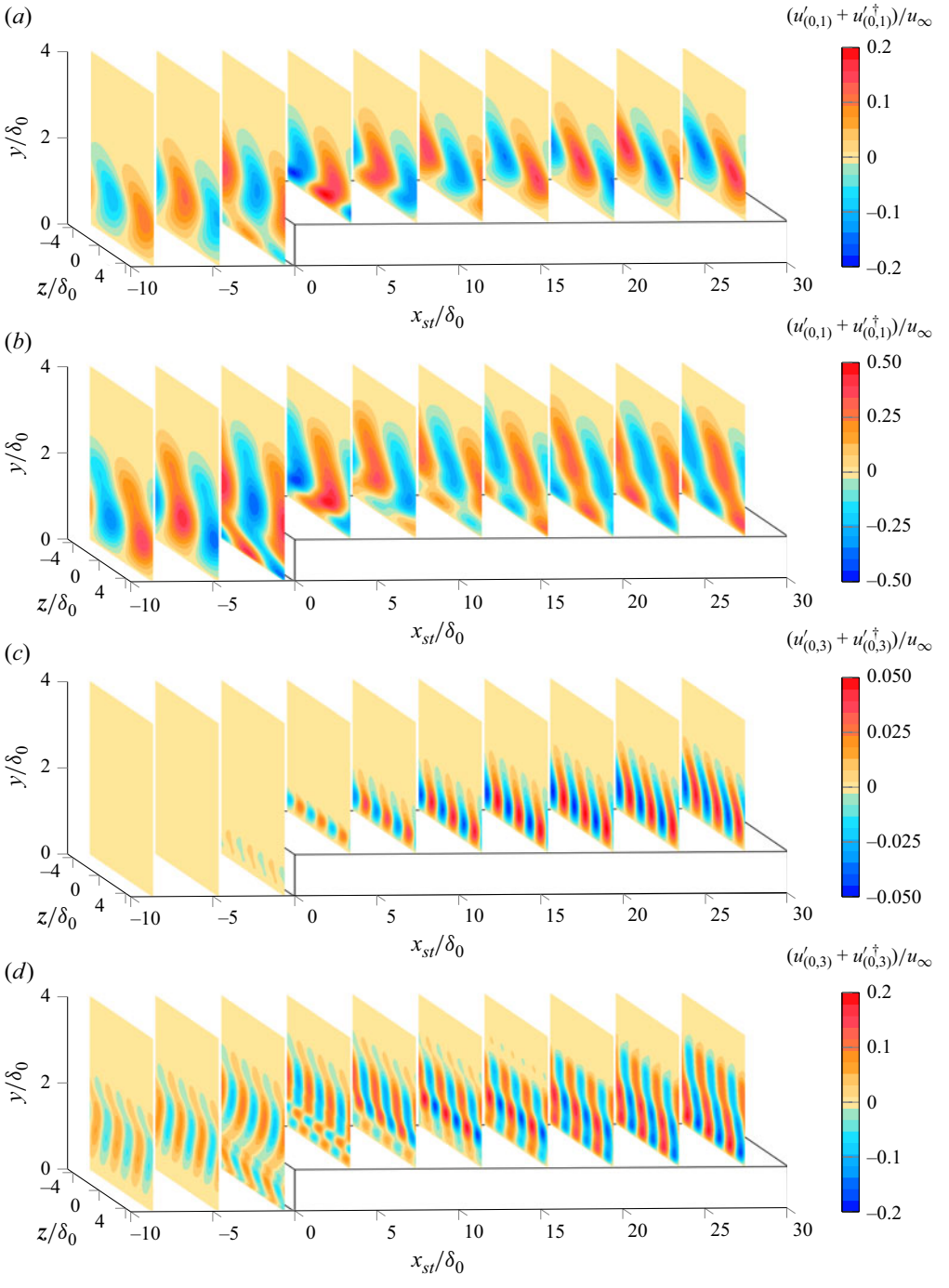


Figure 6. Organisation of stationary spanwise perturbation modes in the medium-amplitude, s.*B* (*a*,*c*), and large-amplitude, s.*C* (*b*,*d*), cases: $\beta = \beta_0$ (*a*,*b*) and $3\beta_0$ (*c*,*d*). The incoming modes in (*c*) are invisible due to their small amplitude compared with modes downstream of the step.

https://doi.org/10.1017/jfm.2026.11854 Published online by Cambridge University Press

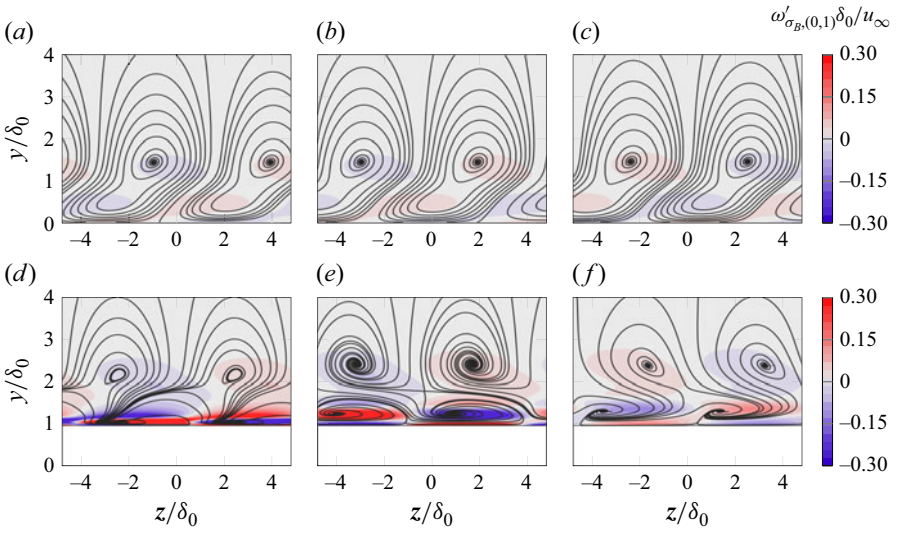


Figure 7. Organisation of the stationary fundamental spanwise perturbation mode in the y–z plane, shown via perturbation vorticity, $\omega'_{x\sigma_B,(0,1)}$ (colour) with projected streamlines of the perturbation velocity components $v'_{(0,1)}$ and $w'_{\sigma_B,(0,1)}$. (*a–c*) No-step case r.*B* and (*d–f*) step case s.*B* at $x_{st}/\delta_0 = 0.3$ (*a*,*d*), 2.6 (*b*,*e*) and 7.6 (*c*,*f*).

to small-wavelength perturbations (Eppink 2020; Casacuberta *et al.* 2022*b*). In contrast, case s.*C* (figure 8*f*) exhibits a significant stabilisation of the $\beta = 2\beta_0$ component and a reordering of the modal energetic hierarchy, relative to the reference no-step case. This disorderly evolution suggests that the influence of the step on incoming stationary perturbations cannot be simply interpreted as a uniform amplification (or attenuation) of the stationary crossflow vortex as a whole.

5.2. *Mechanisms of energy transfer*

In § 3, energy-balance equations for stationary spanwise perturbation modes were formulated. The framework developed in § 3 is employed in this section to assess the effects of incoming perturbation amplitude on the mechanisms of interaction between stationary perturbations and the step. As described previously, each term in (3.4) characterises a mechanism contributing to the time rate of change of kinetic energy within a spanwise-harmonic perturbation space. In this present context, the term perturbation space refers to the combination of a stationary spanwise perturbation mode and its complex conjugate, i.e. $\boldsymbol{v}'_{(0,n)} + \boldsymbol{v}'_{(0,-n)}$, $n = 0, 1, \ldots, N$ (§ 3). For the analysis of this section, the stationary perturbation decomposition is truncated at $N = 20$ (2.3). The methodology is first exemplified under medium-amplitude CFI conditions by comparing the step and no-step scenarios. The analysis is then extended to large-amplitude CFI conditions.

First, consider reference (no-step) conditions and the fundamental space $n = 1$, corresponding to perturbations with $\beta = \beta_0$. The spatial evolution of the terms of (3.4) is shown in figure 9(*a–c*). Production adds the dominant positive contribution (figure 9*a*), where $\mathcal{P}_{\beta_0} > 0$ indicates kinetic energy transfer from the unperturbed base flow to the primary-wavelength perturbations. Nonlinear interactions contribute negligibly to the energy budget (figure 9*c*), consistent with the agreement between solutions from the linear and nonlinear PSE approach in this x region (figure 3*b*). Viscous effects and advection are the main mechanisms balancing out the production of kinetic energy, i.e. $\mathcal{D}_{\beta_0} + \mathcal{T}_{\beta_0} < 0$.

https://doi.org/10.1017/jfm.2026.11854 Published online by Cambridge University Press

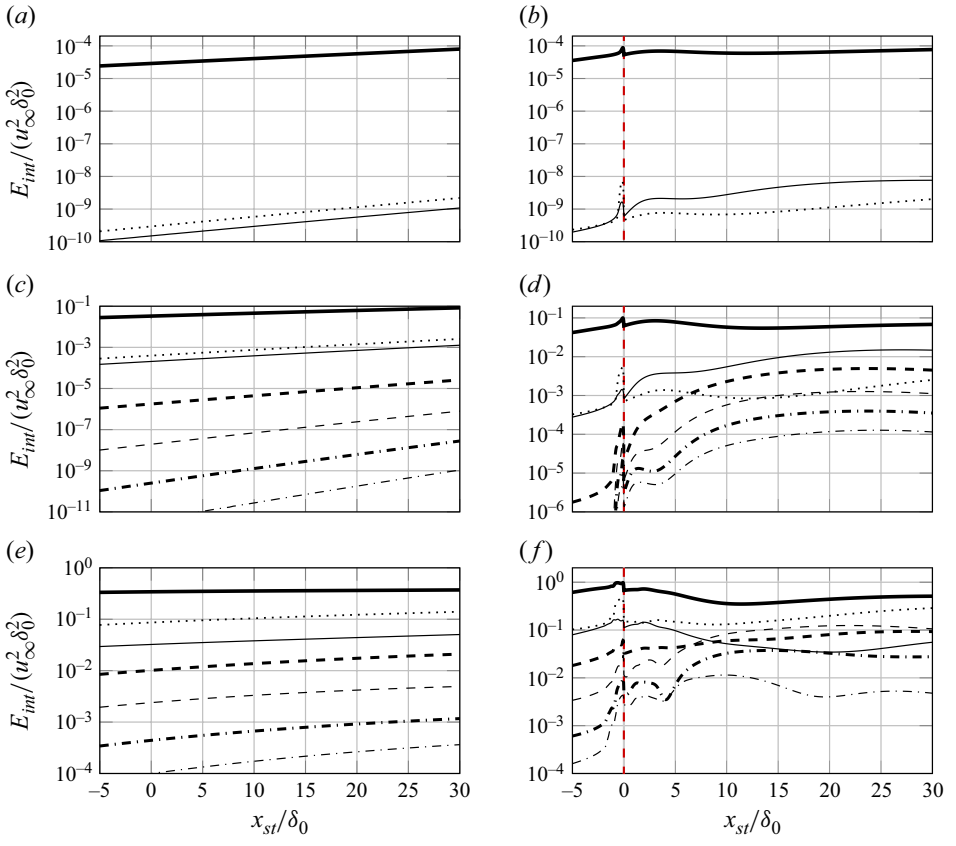


Figure 8. Evolution in x of the kinetic energy of spanwise-harmonic perturbation spaces, $E_{int} = \int E_{n\beta_0}\,\mathrm{d}y$ (3.2), for $n = 0$ (dotted lines), 1 (thick solid lines), 2 (thin solid lines), 3 (thick dashed lines), 4 (thin dashed lines), 5 (thick dash-dotted lines), 6 (thin dash-dotted lines). The small-amplitude r.A (a) and s.A (b) cases, the medium-amplitude r.B (c) and s.B (d) cases and the large-amplitude r.C (e) and s.C (f) cases, are shown. Note that panels (a, b) and (e, f) use identical ordinate scaling within each pair, while the scaling differs between pairs and between panels (c, d). The vertical dashed line indicates the step location.

This interplay between perturbation mechanisms is typically reversed in the high-order perturbation spaces, $n > 1$, with the analysis still strictly confined to reference (no-step) conditions. Specifically, perturbation growth is primarily driven by nonlinear interactions, $\mathcal{N}_{n\beta_0}$, $n > 1$, whilst linear production, $\mathcal{P}_{n\beta_0}$, $n > 1$, contributes in a stabilising manner. Figure 10(a–c) illustrates this behaviour for $n = 3$, which is representative of the high-order harmonic perturbation spaces in case r.B. The quantitative impact of individual perturbation spaces is characterised in figure 11(a–e), which presents the integral contribution of the terms of (3.4) over a domain S defined by $-20 \leqslant x_{st}/\delta_0 \leqslant 30$ and $y/\delta_0 \leqslant 6$.

The presence of the step significantly alters the mechanisms of kinetic energy transfer of stationary perturbations. Under medium-amplitude CFI conditions, the inclusion of the step causes production to act locally stabilising at the step in the space $n = 1$. This is indicated by the red contour in figure 13(a) signifying $\mathcal{P}_{\beta_0} < 0$. This phenomenon has been associated to a reverse lift-up effect (Casacuberta *et al.* 2024). Conversely, the opposite trend is observed for high-order harmonic perturbation spaces. That is, under reference

https://doi.org/10.1017/jfm.2026.11854 Published online by Cambridge University Press

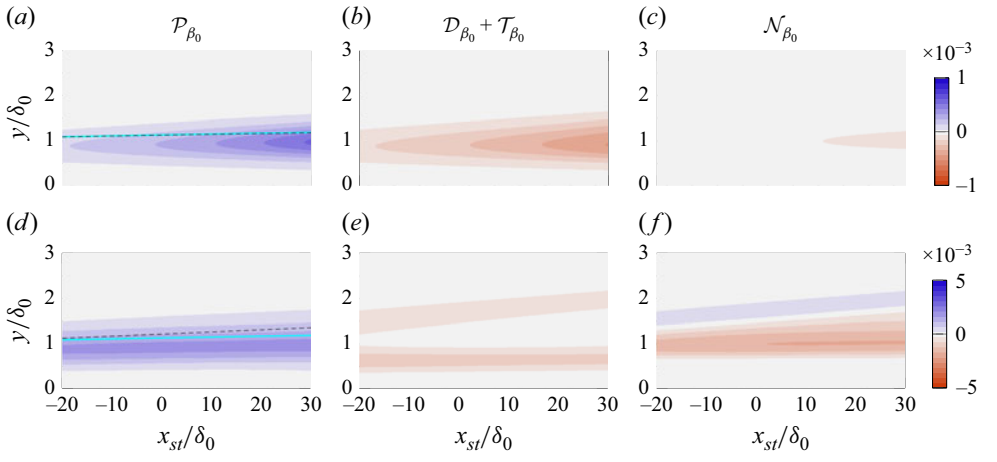


Figure 9. Spatial evolution of budget terms of (3.4) for $n = 1$ in cases r.*B* (top) and r.*C* (bottom): (*a*,*d*) energy production, (*b*,*e*) viscous effects and energy advection, (*c*,*f*) work of nonlinear interactions. Loci of crossflow inflection points in the base flow (solid cyan line) and by the addition of the mean-flow distortion (dashed black line) in (*a*,*d*).

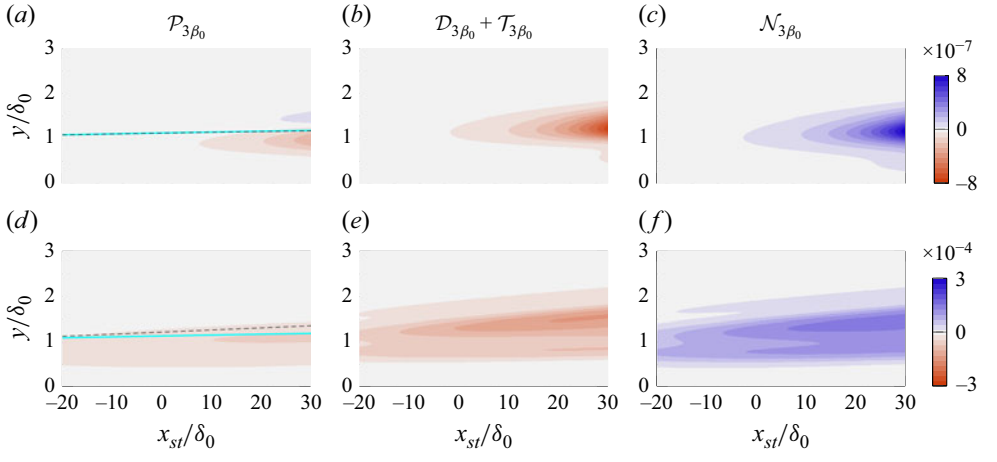


Figure 10. Spatial evolution of budget terms of (3.4) for $n = 3$ in cases r.*B* (top) and r.*C* (bottom): (*a*,*d*) energy production, (*b*,*e*) viscous effects and energy advection, (*c*,*f*) work of nonlinear interactions. Loci of crossflow inflection points in the base flow (solid cyan line) and by the addition of the mean-flow distortion (dashed black line) in (*a*,*d*).

(no-step) conditions, production yields a stabilising contribution (figures 10*a–c*, 11*d* and 11*e*), whereas it acts destabilising at the step (figures 12*d,* 12*e* and 14*a–c*).

Previous studies have argued that the step flow destabilises stationary perturbations through an inflectional mechanism (Eppink 2020). More recently, linear stability analysis has confirmed this by identifying an unstable stationary eigensolution of the base-flow profiles (Casacuberta *et al.* 2022*b*), albeit it emerges exclusively for $\beta > \beta_0$, within the x range where the profiles downstream of the step develop an inflection point near the wall. It is noted that the flow environment of Casacuberta *et al.* (2022*b*) is identically case s.*B* here. The results from the linear stability analysis of Casacuberta *et al.* (2022*b*) reconcile with the present observation that linear production of high-order harmonic perturbations

https://doi.org/10.1017/jfm.2026.11854 Published online by Cambridge University Press

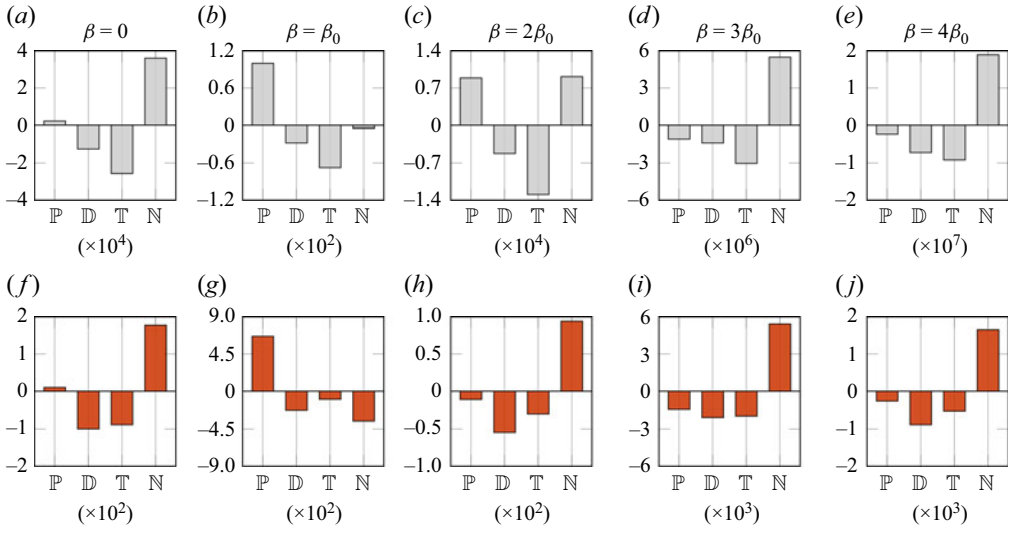


Figure 11. Integral contribution over S of budget terms of (3.4) in cases r.B (top) and r.C (bottom) for $n = 0$ (a,f), 1 (b,g), 2 (c,h), 3 (d,i), 4 (e,j). Blackboard bold symbols denote quantities integrated over S.

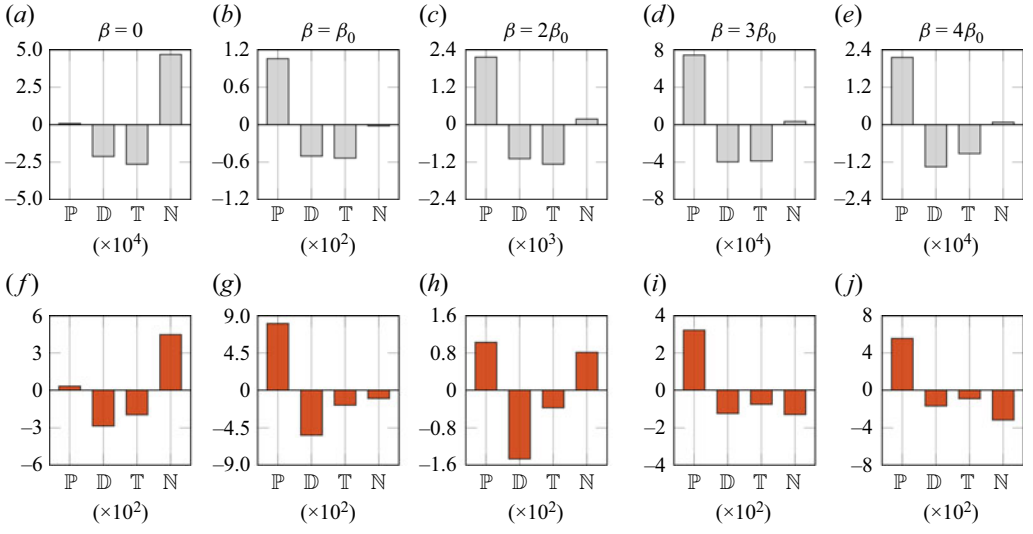


Figure 12. Integral contribution over S of budget terms of (3.4) in cases s.B (top) and s.C (bottom) for $n = 0$ (a,f), 1 (b,g), 2 (c,h), 3 (d,i), 4 (e,j). Blackboard bold symbols denote quantities integrated over S.

peaks at the location of step-induced inflection points (see figure 14(a) illustrating $\mathcal{P}_{3\beta_0}$ for reference). The cyan lines in figure 14(a) mark the loci of inflection points in the crossflow profile of the unperturbed base flow; the lower branch is exclusive to step conditions, as evident from the comparison with figure 10(a).

Amplitude effects on energy-transfer mechanisms at the step are next assessed by extending the analysis to large-amplitude CFI conditions. Specifically, the reference (no-step) case r.C is characterised in figures 9(d–f) and 10(d–f), illustrating the perturbation spaces $n = 1$ and 3, respectively. The step case s.C is characterised in figures 13(d–f) and 14(d–f), also illustrating the perturbation spaces $n = 1$ and 3. The

https://doi.org/10.1017/jfm.2026.11854 Published online by Cambridge University Press

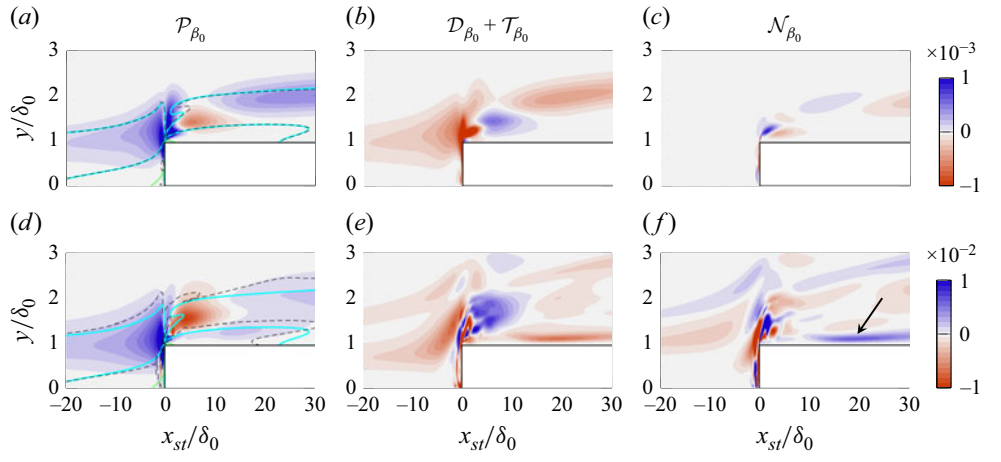


Figure 13. Spatial evolution of budget terms of (3.4) for $n = 1$ in cases s.B (top) and s.C (bottom): (a,d) energy production, (b,e) viscous effects and energy advection, (c,f) work of nonlinear interactions. Loci of crossflow inflection points in the base flow (solid cyan line) and by the addition of the mean-flow distortion (dashed black line) and base-flow reversal $u_B = 0$ (dotted green line) in (a,d).

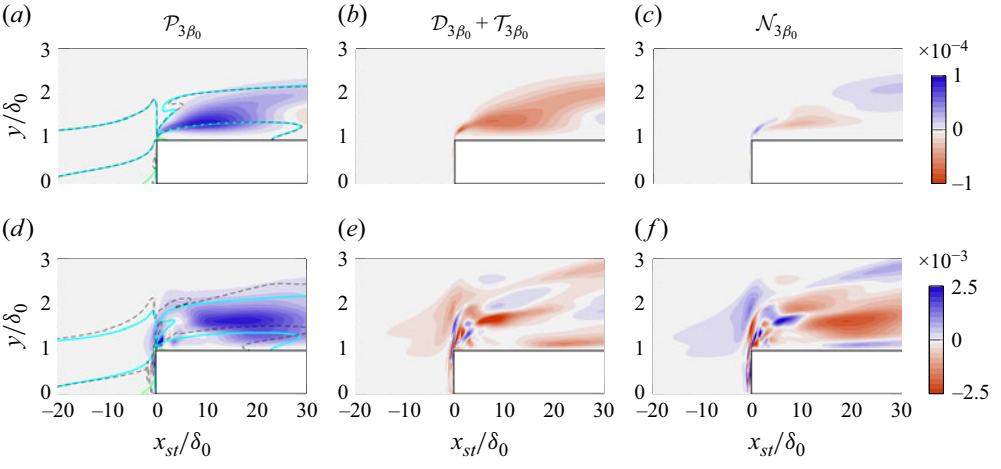


Figure 14. Spatial evolution of budget terms of (3.4) for $n = 3$ in cases s.B (top) and s.C (bottom): (a,d) energy production, (b,e) viscous effects and energy advection, (c,f) work of nonlinear interactions. Loci of crossflow inflection points in the base flow (solid cyan line) and by the addition of the mean-flow distortion (dashed black line) and base-flow reversal $u_B = 0$ (dotted green line) in (a,d).

corresponding energy budgets are presented in figure 11(f–j) for reference (no-step) conditions and figure 12(f–j) for step conditions.

Overall, case r.C exhibits a qualitatively similar behaviour to case r.B. That is, energy production drives the amplification of the fundamental CFI mode ($\beta = \beta_0$; figure 11g), while nonlinear interactions drive the amplification of high-order harmonic CFI modes ($\beta > \beta_0$; figure 11h–j). However, as expected, for a stronger stationary crossflow vortex, the nonlinear interactions acting on individual modes are overall more pronounced in case r.C compared with case r.B (figure 11).

With the step present, high-order perturbation modes destabilised analogously by the inflectional instability at the step (§ 5.1) exhibit a similar rate of growth in figure 8(d); i.e.

https://doi.org/10.1017/jfm.2026.11854 Published online by Cambridge University Press

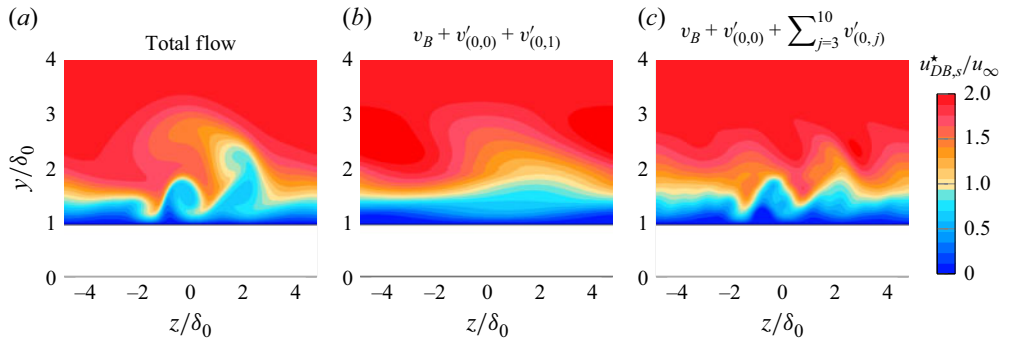


Figure 15. Topology of steady flows illustrated by z–y planes at $x_{st}/\delta_0 = 9.4$ of velocity $u^{\star}_{DB,s}$. The symbol $\star$ indicates that the flow is built considering the superposition of unperturbed base flow, $\boldsymbol{v}_B$, and different numbers of spanwise modes, j: (*a*) total flow $u_{DB,s}$, (*b*) modes $j = 0$, 1, (*c*) modes $j = 0$, 3–10.

representing the medium-amplitude case s.*B*. While the same inflectional mechanism is also present in the large-amplitude case s.*C*, it is observed that the spanwise mode $\beta = 2\beta_0$ undergoes significant stabilisation in x downstream of the step (figure 8*f*). The present energy-balance analysis enlightens that the mechanism of production at the step (i.e. reflecting the imprint of the inflectional instability) is notably weaker in the perturbation space $n = 2$, compared with $n > 2$, under large-amplitude CFI conditions.

A key result of the present analysis is that, in addition to this linear mechanism, nonlinear effects significantly contribute to the deformation of the near-wall-shear layer downstream of the step in case s.*C*. To illustrate this, consider first the perturbation space $n = 1$. An elongated contour of $\mathcal{N}_{\beta_0} > 0$, i.e. signifying a destabilising contribution of nonlinear interactions, emerges near the wall from $x_{st}/\delta_0 = 10$ (see the arrow in figure 13*f*). This feature is absent in cases s.*A* and s.*B*. In case s.*C*, the elongated contour of $\mathcal{N}_{\beta_0} > 0$ spatially coincides with the location where the near-wall streaks of fundamental wavelength – initially generated at the upper step corner – amplify in x following a brief phase of spatial stabilisation (figure 6*b*). By contrast, in case s.*B* the corresponding streaks vanish rapidly in x (figure 6*a*). In results not shown here, a structurally similar elongated contour of the nonlinear mechanism is found to manifest also in the perturbation space $n = 0$, i.e. the non-oscillatory component $\beta = 0$, and in the higher-order perturbation spaces such as $n = 3$, 4, 5. The strength of $\mathcal{N}_0 > 0$ in this region is comparable to that of $\mathcal{N}_{\beta_0} > 0$ and exceeds that of the higher harmonics.

The spatial amplification of high-order harmonic perturbation streaks initially induced at the upper step corner (see Casacuberta *et al.* (2025, § IV.D) for a description of this phenomenon) spatially correlates with regions of positive $\mathcal{N}_{n\beta_0}$ near the wall for $n > 2$. This is illustrated in figures 6(*d*) and 14(*f*) for $n = 3$. Confirmation of a significant growth of the mean-flow distortion (i.e. mode $\boldsymbol{v}'_{(0,0)}$ (2.3)) at the step in case s.*C* is provided by the pronounced alteration of the underlying flow topology near the wall. This is apparent when comparing the fields $\boldsymbol{v}_B$ and $\boldsymbol{v}_B + \boldsymbol{v}'_{(0,0)}$, as illustrated by the different organisation of solid cyan and dashed black lines in figure 14(*d*). These lines represent, respectively, the loci of inflection points in the crossflow profile of the unperturbed base flow, $\boldsymbol{v}_B$, and the modified flow $\boldsymbol{v}_B + \boldsymbol{v}'_{(0,0)}$. Thus, the present results suggest that a nonlinear perturbation effect is responsible for the spatial amplification of the near-wall streaky structures (assessed up to perturbation space $n = 6$) and the mean-flow distortion sufficiently downstream of the step.

https://doi.org/10.1017/jfm.2026.11854 Published online by Cambridge University Press

Overall, the dominant perturbation mechanisms at the step under large-amplitude CFI conditions (i.e. case s.C) are summarised as follows.

(i) A spatial stabilisation of the fundamental CFI due to a linear effect; specifically, the reversal of the mechanism of production close downstream of the step confirming the reverse lift-up effect of Casacuberta *et al.* (2024).
(ii) A nonlinear spatial amplification of near-wall perturbation streaks that are initially induced at the upper step corner by a linear non-modal mechanism (Casacuberta *et al.* 2025). These streaks appear for every spanwise perturbation mode, and a subset of them – at least up to the sixth spanwise mode – undergo nonlinear amplification in x.
(iii) A selective destabilising influence of a family of step-induced inflectional profiles to perturbations with $\beta \leqslant 2\beta_0$ (non-active) versus $\beta > 2\beta_0$ (active). This mechanism induces a reordering of the energetic hierarchy of high-order harmonic spanwise perturbation modes, compared with reference (no-step) conditions.

To conclude, the inception of the novel CS dip at the step, i.e. the stationary flow structure developing due to the step, previously introduced in figure 4(f), is primarily attributed to the mechanisms (ii) and (iii) above. By leveraging the decomposition of the perturbation field into spanwise modes, a low-order reconstruction has been performed. The skeleton of the CS dip emerges from the superposition of modes within the range $3\beta_0 \leqslant \beta \leqslant 10\beta_0$ (see figure 15). As described above, these modes are subject to the linear destabilising effect of the inflectional mean-flow profiles farther from the wall and to the mechanism of nonlinear streak amplification in the near-wall region.

6. Unsteady flow evolution

The analysis is extended to unsteady mechanisms and breakdown of the laminar flow at the step. In the pertinent simulations, the flow is forced in time at selected temporal frequencies (§ 2.3) and the evolution of unsteady perturbations is monitored accordingly. The DNS results are complemented by two-dimensional linear secondary stability analysis performed on the steady perturbed flow.

6.1. *Mean skin friction*

First, an overview of the cases is provided using mean-flow metrics. More specifically, the time- and spanwise-averaged skin-friction coefficient is used to segregate between laminar and turbulent regimes. This is evaluated as

$$\langle C_f \rangle = \left\langle \frac{\overline{\tau_w}}{\frac{1}{2}\rho u_\infty^2} \right\rangle, \tag{6.1}$$

where $\overline{\tau_w}$ denotes the time-averaged wall-shear stress, ρ is the density and $\langle\cdot\rangle$ expresses spanwise-averaging operation. The skin-friction coefficient is normalised using the characteristic velocity u_∞ for consistency with the global scaling adopted in this work. The chordwise evolution of $\langle C_f \rangle(x)$ (6.1) is illustrated in figure 16. Black empty circles characterise the large-amplitude reference case $r.C$. The significant increase of $\langle C_f \rangle$ towards the end of the domain signifies the breakdown of the stationary crossflow vortices. In case r.C, the laminar–turbulent transition front is approximately located at 40 % of the chord of the wing model used to guide the DNS set-up (Rius-Vidales & Kotsonis 2021), i.e. at $x/\delta_0 \approx 400$. When the step is present for an identical amplitude of incoming stationary crossflow vortices, i.e. case s.C, the transition front shifts to a position immediately

https://doi.org/10.1017/jfm.2026.11854 Published online by Cambridge University Press

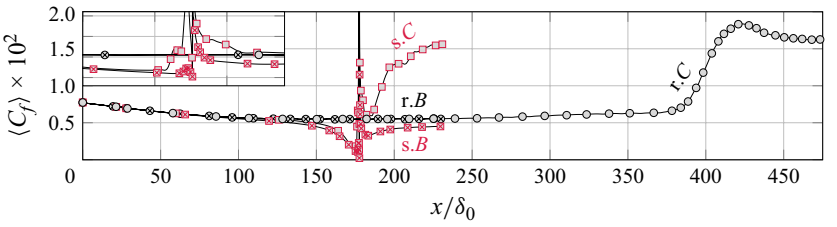


Figure 16. Chordwise evolution of the spanwise- and time-averaged skin-friction coefficient in the medium-amplitude cases r.*B* (black circles with a cross) and s.*B* (red squares with a cross), and large-amplitude cases r.*C* (black empty circles) and s.*C* (red empty squares). Vertical line indicates the step location, and the top inset provides a zoomed-in view over the range $170 \leqslant x/\delta_0 \leqslant 184$.

downstream of the step (see red empty squares in figure 16). However, this does not apply to the low- and medium-amplitude cases s.*A* and s.*B*.

Experimental work has shown that subcritical (i.e. negligible), critical (i.e. notable) and supercritical (i.e. drastic) movements of the transition front upstream correlates with an increase in the step height for a fixed amplitude of incoming stationary crossflow vortices (Rius-Vidales & Kotsonis 2021). The results of the present work additionally illustrate that the categorisation of transition regimes in swept-wing flow due to a forward-facing step is not uniquely set by the step height. The amplitude of incoming crossflow vortices plays a main role as well. This is also supported by previous experiments (Eppink 2020).

6.2. *Mechanisms of unsteady perturbations*

Prior to examining how the step influences unsteady perturbations, an overview of their evolution under reference (no-step) conditions is presented. The amplitude function of perturbation modes $\boldsymbol{v}'_{(k,j)}$ (2.3) is recovered following the procedure described in § 2.3. For case r.*C*, figure 17 shows the metric

$$\left[A_k^u\right] = \max_y \left(\sqrt{\sum_{j=0}^{9} |\tilde{u}|^2_{(k,j)}} \right), \tag{6.2}$$

which expresses the amplitude of perturbations with a temporal frequency of $k = 1$–8 kHz.

Previous work by the authors' group has shown that transition in the present case r.*C* is driven by the type-I secondary CFI (Casacuberta *et al.* 2023). From approximately $x/\delta_0 = 360$, unsteady large-scale structures, typically associated with the growth of the type-I mechanism, emanate from the upwelling region of the original stationary crossflow vortices; see Wassermann & Kloker (2002) and Casacuberta *et al.* (2022*a*) for a graphical representation of these flow structures. Figure 17 shows that perturbations with a temporal frequency of $f = 3$ kHz attain the largest amplitude in the region $x/\delta_0 > 360$, despite higher-frequency components exhibiting larger growth rates (Casacuberta *et al.* 2023).

The mechanisms of unsteady instability at the step are first assessed quantitatively through temporal probe data, i.e. pointwise measurements of instantaneous velocity. The analysis is restricted to case s.*C*, where laminar breakdown occurs just downstream of the step. The CFI-step dip of low momentum (CS dip; see figure 4), previously identified in the steady deformation of the shear layer by the step (§ 4), will be shown to be a primary source of unsteady activity. The PSD of time-resolved probe data is presented in figures 18(*b*) and 18(*c*) at three different x locations immediately downstream of the step, but upstream of laminar breakdown.

https://doi.org/10.1017/jfm.2026.11854 Published online by Cambridge University Press

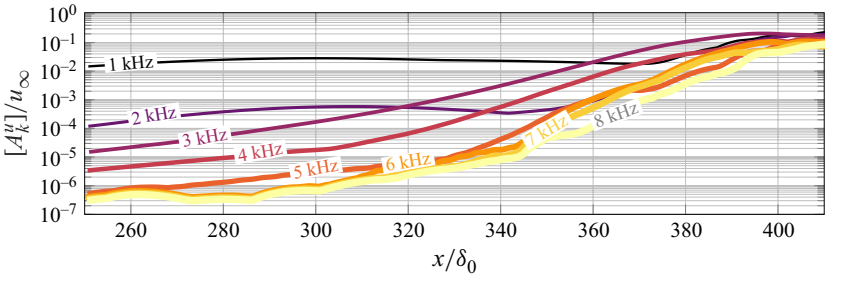


Figure 17. Chordwise evolution of the amplitude of unsteady perturbation modes from DNS for case r.C at temporal frequencies $f = 1$–8 kHz, in steps of 1 kHz (thin-to-thick and dark-to-bright colours indicate increasing frequency).

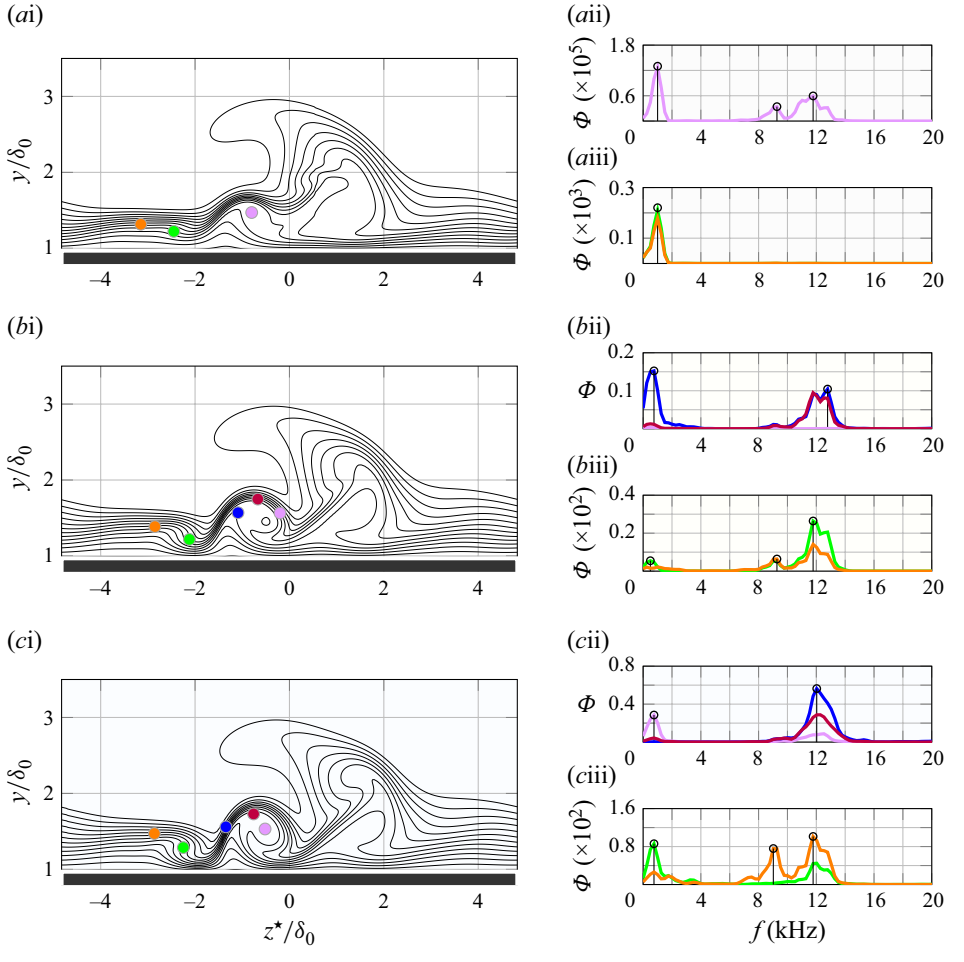


Figure 18. Topology of the steady perturbed flow in case s.C (i) and PSD, Φ (in units of $u_\infty \delta_0$), of temporal probe data (ii,iii) identified by the same colour of a corresponding probe at $x_{st}/\delta_0 = 5$ (a), 8 (b), 10 (c). Contours in (ai–ci) are isolines of $u_{DB,s}$ ranging from 0 to $1.5u_\infty$. The coordinate $z^\star$ indicates a spanwise shift relative to the intersection between the CS dip and the stationary crossflow vortex.

https://doi.org/10.1017/jfm.2026.11854 Published online by Cambridge University Press

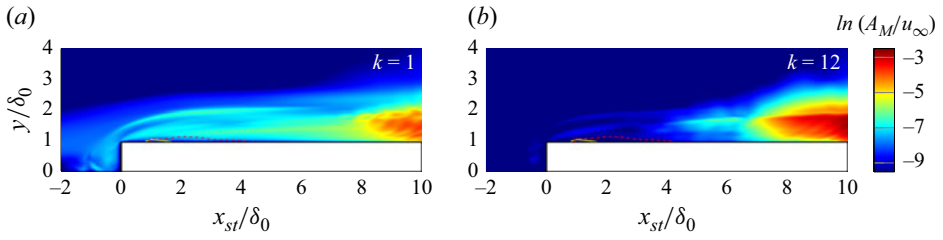


Figure 19. Amplitude functions of unsteady perturbation modes: 1 kHz (*a*), 12 kHz (*b*), where $A_M = \sqrt{\sum_{j=-13}^{13} |\tilde{u}|^2_{(k,j)}}$. Flow reversal ($u_{DB} = 0$) in planes of the steady perturbed flow at $z/\delta_0 = -1.7$ (yellow solid line) and $z/\delta_0 = 4.8$ (red dotted line).

Unsteady perturbation content at the step appears in both the low-frequency band, peaking at $f \approx 1$ kHz, and in the high-frequency band, peaking at $f \approx 9$ kHz and $f \approx 12$ kHz. Perturbations at $f \approx 12$ kHz primarily develop along the inclined lateral shear layer of the CS dip (see dark blue probe in figure 18), whereas those at $f \approx 9$ kHz are concentrated along the shear layer adjacent to the CS dip on the left-hand side (see orange probe in figure 18). While low-frequency perturbations initially dominate at upstream locations (figure 18*a*), high-frequency perturbations progressively become dominant further downstream (figures 18*b* and 18*c*). This trend is further illustrated by the amplitude function (2.3) of perturbation modes at individual frequencies of $f = 1$ kHz (*a*) and 12 kHz (*b*), characterised as $\sqrt{\sum_{j=-13}^{13} |\tilde{u}|^2_{(k,j)}}$, $k = 1$, 12 in figure 19. Consistent with the probe analysis, figure 19 shows that higher-frequency perturbations exhibit larger spatial growth rates. Overall, perturbations at $f = 12$ kHz eventually attain the largest amplitude downstream of the step.

It may be postulated that the low-frequency unsteadiness at the step represents a manifestation of a type-III secondary CFI, as supported by the organisation of the perturbation shape of the $f = 1$ kHz component. A potential mechanism involving flapping or breathing of the shear layer at the step (Eppink 2020), which could contribute to the low-frequency unsteadiness, is not evident in the DNS.

Conversely, the present results provide evidence suggesting that the high-frequency perturbations at the step originate from a shear-layer instability, as also proposed by Eppink (2020). First and foremost, a correlation is observed between the spatial organisation of major unsteady perturbation structures and the strong shear layer formed by the CS dip. This is illustrated in figure 20(i) depicting the instantaneous organisation of the $f = 12$ kHz unsteady perturbation field (i.e. characterised as $\sum_{j=-13}^{13} \tilde{u}_{(12,j)} e^{i(j\beta_0 z)} + \tilde{u}_{(-12,j)} e^{i(j\beta_0 z)}$) in relation to the embedding flow. As the CS dip develops along the chordwise direction, the unsteady perturbation gradually shifts towards its laterally inclined shear layer; see figures 20(*b*i) and 20(*c*i). It will be shown in § 6.3 that large-scale vortex shedding emanates from this upwelling region of the CS dip.

Second, two-dimensional linear secondary stability analysis (detailed in § 2.4) of the steady perturbed flow identifies three eigenmodes that are explosively unstable at high frequencies (9–12 kHz), and do not manifest under reference (no-step) conditions. These modes are henceforth referred to as the CS modes. Perturbation shapes corresponding to the most unstable instances are shown in figure 21, with further characteristics reported in table 3. Initially in x, the CS modes are positioned above the reverse-flow region and are mutually distinguished by forming 1, 2 and 3 local regions where $|\tilde{u}_{BiG}|$ is large in z, corresponding to their mode index. We qualify the CS-mode growth rates ($-\alpha_{\theta,i}\delta_0 \sec\theta$ in

https://doi.org/10.1017/jfm.2026.11854 Published online by Cambridge University Press

CS mode	Method	f (kHz)	x_{st}/δ_0	θ (°)	$-\alpha_{\theta,i}\delta_0 \sec\theta$	$\lambda_{x_\theta}/\delta_0$	c_{ph}/u_∞	c_g/u_∞
1	Local	12	1.185	−53.1	3.437	1.144	0.701	0.419
1	{Plane-marching}	12	1.185	−53.1	3.636	1.131	0.693	0.383
2	Local	11	2.185	−43.1	1.775	1.332	0.7482	0.581
3	Local	9	2.485	−41.5	1.207	1.737	0.798	0.639

Table 3. Most unstable ($\max_x\{-\alpha_{\theta,i}\sec\theta\}$) CS-mode characteristics for the frequencies that result in the largest N factors at $x_{st}/\delta_0 = 10$, obtained with the local or plane-marching ($s = 0.5\delta_0$) stability approach.

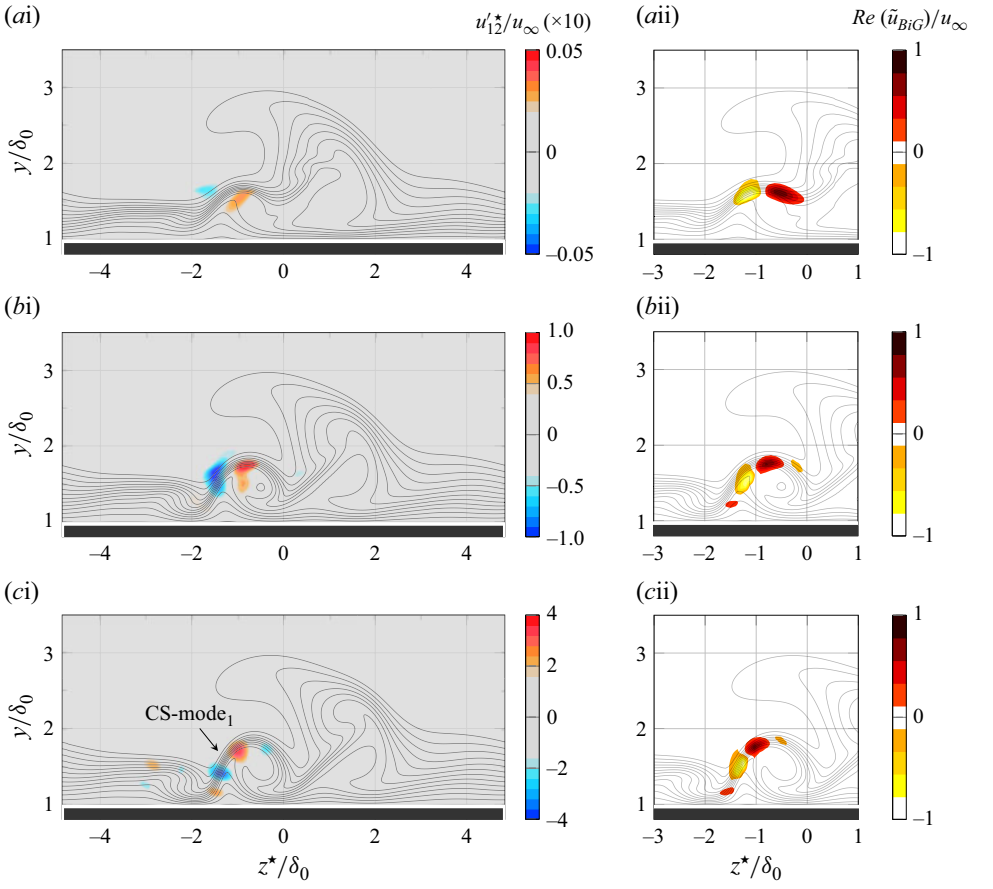


Figure 20. Organisation of the $f = 12$ kHz unsteady perturbation field, where $u'^{\star}_{12} = \sum_{j=-13}^{13} \tilde{u}_{(12,j)}e^{i(j\beta_0 z)}/u_\infty + \tilde{u}_{(-12,j)}e^{i(j\beta_0 z)}/u_\infty$, in case s.$C$ from DNS (ai–ci) and the real part of the perturbation shape obtained from the local stability approach (aii–cii) at $x_{st}/\delta_0 \approx 5$ (a), 8 (b), 10 (c). Topology of the steady perturbed flow portrayed as isocontours of u_{DB}/u_∞ (ranging from 0 to $1.5u_\infty$) by solid lines in (a, b).

table 3) as explosive upon noting that they are a factor 35 larger than the maximum growth rates achieved by the classic secondary crossflow instabilities for no-step conditions. Table 3 furthermore specifies the perturbations' wavelength, λ_{x_θ}, phase speed c_{ph} and group speed c_g all in the direction of the crossflow vortex (i.e. in the non-orthogonal x_θ direction), which are defined as

https://doi.org/10.1017/jfm.2026.11854 Published online by Cambridge University Press

Method	s/δ_0	CS mode f (kHz)	1 9	1 11	1 12	1 13	2 9	2 11	2 12	3 9	3 12
Local	–	N	14.90	17.35	17.68	17.32	8.79	9.56	9.53	5.64	4.63
plane marching	0.5	N	—	17.01	17.39	16.94	—	—	—	—	—
	1.0	N	—	—	17.16	—	—	—	—	—	—
	2.0	N	—	—	16.91	—	—	—	—	—	—

Table 4. Linear amplification N factors at $x_{st} = 10.38\delta_0$ ($x = 188\delta_0$) of unsteady instability eigenmodes based on two-dimensional linear secondary stability analysis.

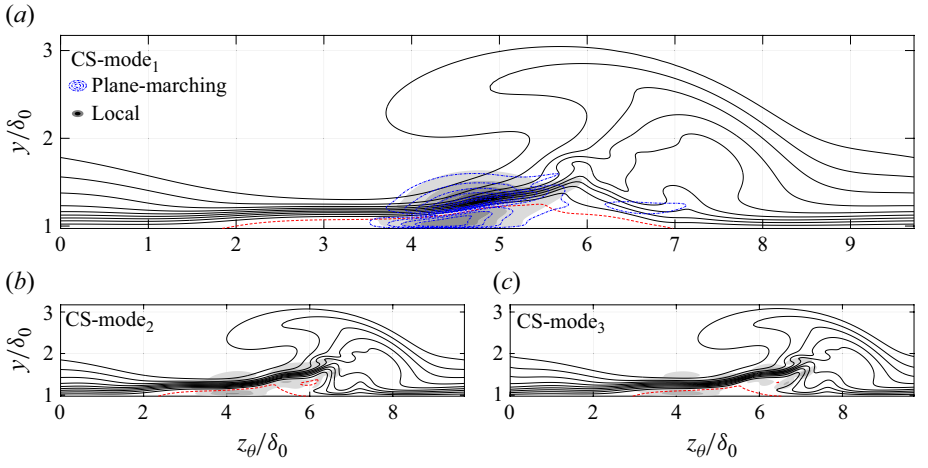


Figure 21. Perturbation shape depicted as $|\tilde{u}_{BiG}|$ isocontours (1/8, 2/8, . . ., 7/8 of $\max_{z,y} |\tilde{u}_{BiG}|$), corresponding to the most unstable instances (x_{st}/δ_0 location corresponding to $\max_x\{-\alpha_{\theta,i} \sec\theta\}$: $x_{st}/\delta_0 = (a)$ 1.19, (b) 2.19, (c) 2.49) of CS modes 1–3 for the frequencies that result in the largest N factors at $x_{st}/\delta_0 = 10$ (details are given in table 3). Isocontours of u_{DB}/u_∞ (solid black lines: 10 %, 20 %, . . ., 90 %; dashed red lines: 0, i.e. flow reversal).

$$\lambda_{x_\theta} = \frac{2\pi}{\alpha_{\theta,r}}; \qquad c_{ph} = \frac{\omega_r}{\alpha_{\theta,r}}; \qquad c_g = \left.\frac{\partial\omega_r}{\partial\alpha_{\theta,r}}\right|_{\alpha_{\theta,i}}. \tag{6.3}$$

where the subscript r denotes the real part.

Large N factors are computed for all CS modes (table 4) at a location upstream of the neutral point of classic type-I and type-II secondary crossflow instabilities ($x/\delta_0 = 188.4$, based on plane-marching results for type II). However, the N factor achieved by CS-mode$_1$ is so much larger than those for CS-mode$_2$ (its relative amplitude is $e^{9.53-17.68} = 10^{-3.5}$) and CS-mode$_3$ ($e^{4.63-17.68} = 10^{-5.7}$), that the remaining analysis focuses on CS-mode$_1$.

The largest amplification factor computed from stability analysis is attained at $f = 12$ kHz (table 4). This result is conform with the results from the DNS probe analysis (figure 18), which indicates that this frequency component dominates in the DNS at similar x positions. The shape function of this critical (i.e. most integrally amplified) stability eigenmode, CS-mode$_1$ in table 4, is ultimately concentrated along the shear layers of the CS dip. This is illustrated in figure 20(ii), which compares the chordwise evolution of the eigenmode, as obtained from the local stability approach, with the perturbation field from

https://doi.org/10.1017/jfm.2026.11854 Published online by Cambridge University Press

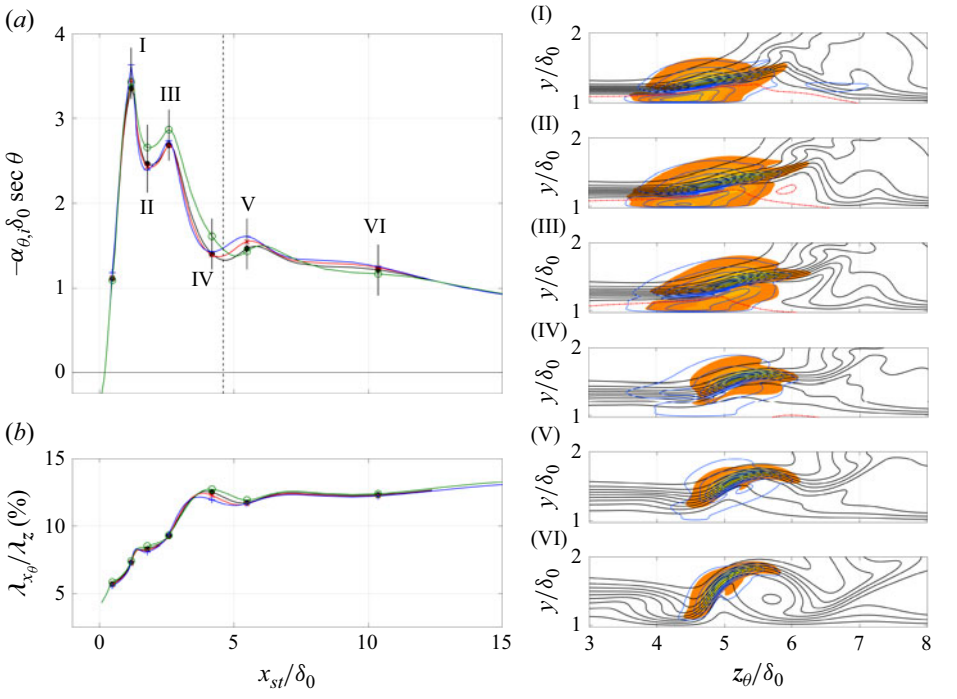


Figure 22. Chordwise evolution of the (*a*) growth rate and (*b*) wavelength of CS-mode$_1$ at 12 kHz as computed with local (green circles) and plane-marching (blue pluses: $s/\delta_0 = 0.5$; red crosses: 1; black dotted: 2) approaches. Maximum extent of reverse flow (black dashed line). Panels (I-VI) show the $|\tilde{u}_{BiG}|$ isocontours ($1/8, 2/8, \ldots, 7/8$ of $\max_{z,y} |\tilde{u}_{BiG}|$) corresponding to CS-mode$_1$ at 12 kHz at x positions indicated in (*a*,*b*) as computed with the local (filled contours) and plane-marching (blue isolines: $s/\delta_0 = 0.5$) approach. Isocontours of u_{DB}/u_∞ (solid black lines: 10 %, 20 %, . . ., 90 %; dashed red lines: 0, i.e. reverse flow).

DNS. Figure 28 in Appendix C further compares the evolution of perturbation amplitude in x between the stability approach and the DNS.

The associated growth rates and chordwise perturbation wavelengths of CS-mode$_1$ from stability analysis are provided in figures 22(*a*) and figure 22(*b*), respectively. This provides evidence that, upstream of the CS dip's development as a large-scale flow structure, CS-mode$_1$ is also significantly destabilised by the local deformation of the flow at the upper step corner, where regions of flow recirculation are present (see figure 22(*a*) in the range $0 \leqslant x_{st}/\delta_0 \leqslant 5$). Further downstream, as it develops, the shape of CS-mode$_1$ resembles the perturbation recovered from DNS (figure 20*c*i), albeit notable differences in the perturbation shape between DNS and the local stability approach are observed during the early stages of the eigenmode development (figures 20i and 20ii).

The stability analysis (see Appendix D) shows that the present flow is convectively, not absolutely, unstable. Following the definition of absolute instability for classic secondary CFI modes (Huerre & Monkewitz 1985, Koch *et al.* 2000, p. 135), the pinching condition is not satisfied, indicating a convective rather than absolute character. Kurz & Kloker (2016) show that the wake of a discrete roughness element in swept-wing flow may support a convective or an absolute instability, the latter arising as the roughness Reynolds number is increased. In the present step flow (see § 6.3), the convective instability alone is sufficient to generate the unsteady vortex shedding downstream of the roughness element that leads to turbulence (Kurz & Kloker 2016). Determining the threshold conditions under which the present configuration would support an absolute instability is left to future work.

https://doi.org/10.1017/jfm.2026.11854 Published online by Cambridge University Press

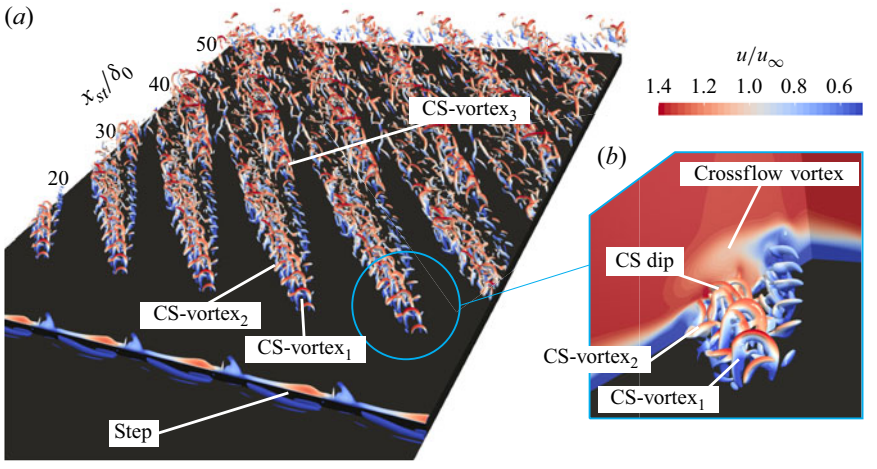


Figure 23. Perspective view of the instantaneous flow organisation at the step for case s.C characterised by the Q-criterion isosurface ($Q\delta_0/u_\infty = 0.8$) coloured with chordwise velocity (a). Zoom with x–y, y–z planes of chordwise velocity (b). In panel (a) the data are duplicated four times in z for illustration purposes.

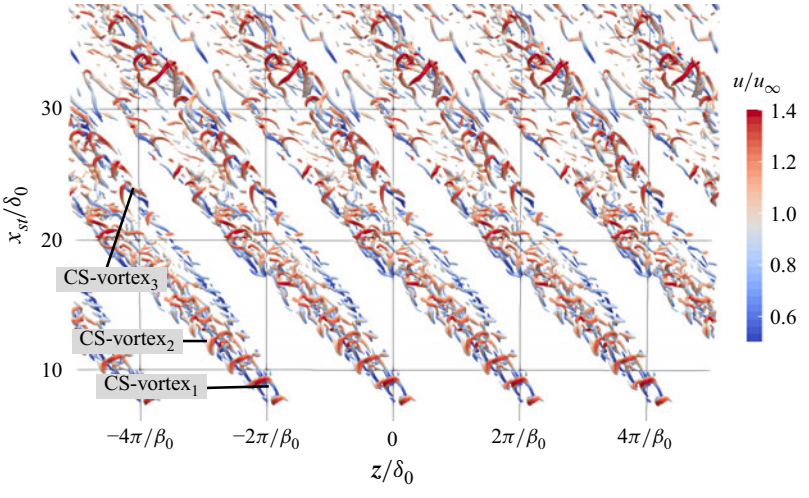


Figure 24. Top view of the instantaneous flow organisation at the step for case s.C characterised by the Q-criterion isosurface ($Q\delta_0/u_\infty = 0.8$) coloured with chordwise velocity. The data are duplicated four times in z for illustration purposes.

6.3. *Instantaneous flow organisation*

The spatial amplification of high-frequency instabilities at the step precedes the shedding of large-scale unsteady vortices, a flow feature manifesting directly at the step only in case s.C. In case s.C the onset of laminar–turbulent transition is marked by spanwise-periodic wedges of unsteady contamination inclined along the crossflow-vortex direction. Figures 23 and 24 illustrate this using Q-criterion isosurfaces (Hunt *et al.* 1988).

Three main families of unsteady vortical structures are identified in the instantaneous flow. First, large-scale hairpin vortices shed from the CS dip, labelled as CS-vortex$_1$ in figure 23. The inception region of CS-vortex$_1$ spatially correlates with the shape

https://doi.org/10.1017/jfm.2026.11854 Published online by Cambridge University Press

of the critical unsteady perturbation, namely CS-mode$_1$ at $f = 12$ kHz, computed by two-dimensional linear secondary stability analysis (§ 6.2). Second, vortical structures of a rather amorphous shape emerge from the shear layer adjacent to the CS dip on the left-hand side and develop spatially near the wall; these are labelled as CS-vortex$_2$ in figure 23. Third, a second family of large-scale hairpin vortices form along the shear layer of the distorted base (see figure 4*f*) of the stationary crossflow vortex; these are labelled as CS-vortex$_3$ in figure 23. The fully developed form of CS-vortex$_3$ appears significantly farther downstream ($x_{st}/\delta_0 > 20$) compared with CS-vortex$_1$ ($x_{st}/\delta_0 \approx 10$), as shown in figures 23 and 24.

We highlight the rapid upward shift of CS-vortex$_1$ and CS-vortex$_3$ in x as a key feature of vortical evolution at the step. This is elaborated as follows: the primary hairpin vortices induced at the CS dip, CS-vortex$_1$, ascend in x towards the upper shear layer of the stationary crossflow vortex. Under reference (no-step) conditions, this upper region is typically associated with the type-II secondary CFI (Malik *et al.* 1999). Similarly, for $x_{st}/\delta_0 > 40$, the secondary hairpin vortices, CS-vortex$_3$, shift upward in x and become immersed in the upper inclined shear layer within the upwelling region of the stationary crossflow vortex (see region labelled as shoulder in figure 4*f*). This shear layer typically feeds growth to the type-I secondary CFI (Malik *et al.* 1999). This effect provides a plausible explanation for the significant unsteady activity measured by Rius-Vidales & Kotsonis (2021) in the boundary-layer region traditionally linked to the classic type-I secondary CFI, albeit the type-I mechanism does not appear in the transitional flow from DNS.

The PSD of temporal probe signals from DNS flattens, signifying turbulence inception, from $x_{st}/\delta_0 = 15$. This trend is quantified in probe measurements taken near the interaction between CS-vortex$_1$ and CS-vortex$_2$, to which we attribute the inception of turbulence in the first place. Probe measurements near CS-vortex$_3$ exhibit spectral flattening at a more downstream location. Thus, both the DNS and the experimental work (Rius-Vidales & Kotsonis 2022) identify that perturbations on the inner side of the crossflow vortex are associated with abrupt laminar–turbulent transition at the step.

7. Discussion on the laminar–turbulent transition route

The classic routes to turbulence in reference wall conditions (i.e. without surface features) are summarised in the well-know diagram of Morkovin *et al.* (1994) (see figure 25*a*). More recently, Crouch (2022) presented an analogous diagram of transition routes for non-ideal walls (i.e. with surface features), shown in figure 25(*b*) with adaptations: a low-disturbance environment is assumed, and the level of surface-induced flow distortion is introduced as a main control parameter. Crouch (2022) redefines the classic path 'A' of Morkovin *et al.* (1994) sub-dividing it into 'A_1', characterising effects of surface receptivity, and 'A_2', characterising the influence of surface-induced modifications on the growth of existing primary eigenmodes. Furthermore, the diagram in figure 25(*b*) proposes that, in the presence of surface features, the transition route switches directly from 'A_1' or 'A_2' to 'E', since transient-growth (or non-modal) effects may occur, but do not alter the transition route (Crouch 2022). The results of this work appear to challenge this claim, as discussed below.

The CS dip is a stationary flow structure that coexists with the stationary crossflow vortex (§ 4). The analysis above has shown that the shear layers surrounding the CS dip support the amplification of secondary unsteady instability eigenmodes if, and only if, the primary incoming CFI has sufficient amplitude. The rapid spatial growth of secondary instabilities ultimately leads to shedding of vortical structures and transition

https://doi.org/10.1017/jfm.2026.11854 Published online by Cambridge University Press

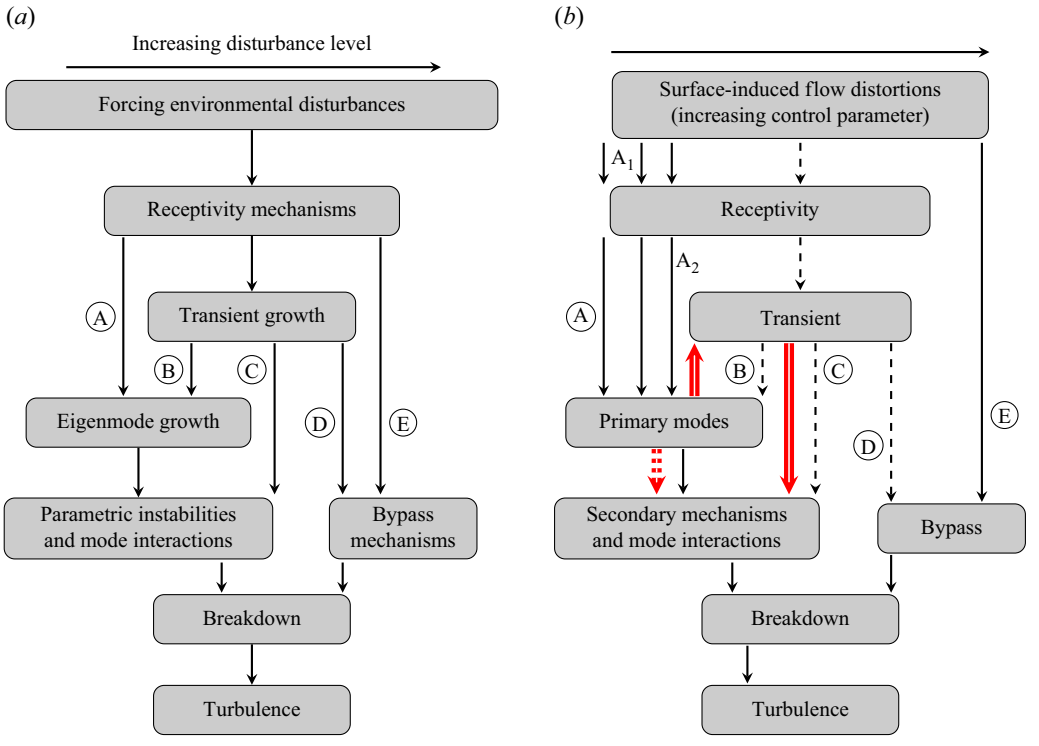


Figure 25. Paths to turbulence in boundary-layer flow as a function of (*a*) the external disturbance level (Morkovin *et al.* 1994) and (*b*) the surface-induced flow distortion in a low-disturbance environment (Crouch 2022). Thick red arrows in (*b*) indicate our new proposed transition path.

to turbulence. Consequently, two flow cases with identical surface step geometry and free-stream receptivity conditions, but differing only in the amplitude of the incoming CFI amplitude, may exhibit fundamentally different transition scenarios. This is demonstrated by case s.*B* (no abrupt transition at the step) versus case s.*C* (abrupt transition at the step).

The analysis of stationary perturbation effects (§ 5) highlights that transition advancement due to the step is influenced by the non-modal growth of stationary perturbation streaks at the step. For specific details on the mechanism responsible for the generation of these non-modal perturbation streaks, the reader is referred to Casacuberta *et al.* (2025). The transition path discussed in this work exhibits a distinctive twofold character. First, the non-modal growth effect manifesting as perturbation streaks at the step originates from the preceding growth of primary eigenmodes, namely the incoming CFI (Casacuberta *et al.* 2025). Second, this non-modal growth only partially sets the conditions for secondary instability development: the destabilisation of the high-order harmonic modes that accompany the fundamental CFI upstream of the step, via an inflectional mechanism, also contribute to this process (§ 5.2). The dual contribution of the incoming CFI in establishing the conditions for secondary mechanisms is illustrated by the red solid and red dotted arrows in figure 25(*b*).

Transition advancement due to the step entails a modification of the transition path, relative to the reference (no-step) scenario (figure 25*b*). The key elements supporting this alteration of the transition path are consistent with wind-tunnel experiments. First, the existence of the CS dip of low momentum is confirmed in time-averaged flow measurements; see Rius-Vidales & Kotsonis (2022, figure 7 II.(*d*)). Rius-Vidales &

https://doi.org/10.1017/jfm.2026.11854 Published online by Cambridge University Press

Kotsonis (2022) further note that the development of the CS dip is specific to the set of experiments exhibiting abrupt transition at the step (cf. their figure 5). This observation aligns with the identification that critical unsteady fluctuations – leading to laminar breakdown – develop spatially in the portion of the shear layer deformed by the CS dip (Rius-Vidales & Kotsonis 2022). Second, Eppink (2020) attributes laminar breakdown at the step to vortex shedding downstream of the reattachment point of the recirculating-flow region, a mechanism also identified by DNS (figures 23 and 24).

Notwithstanding the joint identification of important flow structures between experimental reports and DNS, the nature of the unsteady perturbations that initiate vortex shedding at the step remains an open question. Eppink (2020) attributes the origin of the higher-frequency perturbations to a shear-layer instability, a view supported by the results of this work. Moreover, the spatial evolution of high-frequency unsteady instability eigenmodes – supported by the main shear layers surrounding the CS dip – correlates with key features of the vortex shedding in the present DNS. These findings further align with the primary observations of Rius-Vidales & Kotsonis (2022) that the frequency content and spatial organisation of critical unsteady fluctuations downstream of the step do not reconcile with those of classic secondary crossflow instabilities. This discrepancy implies the presence of a novel unsteady mechanism introduced by the step, as confirmed by the analysis in this work.

8. Conclusions

This work elucidates the mechanisms of instability and breakdown of incompressible swept-wing flow with a forward-facing step in most critical conditions, i.e. where the transition front shifts abruptly just downstream of the step. The analysis is conducted with DNS and complemented by two-dimensional linear secondary stability analysis performed through the local and plane-marching parabolised approaches. The investigation considers a fixed step height while varying the amplitude of the stationary CFI pre-existing upstream of the step. The abrupt-transition regime is realised only for the largest incoming CFI amplitude considered.

The interaction between a sufficiently amplified CFI and the step gives rise to a region of low momentum, termed the CS dip, located in the inner side of the incoming crossflow vortex, beneath its crest. The linear two-dimensional secondary stability analysis has revealed that the region dominated by the CS dip supports the spatial amplification of high-frequency unsteady instability eigenmodes. The temporal frequency and spatial organisation of the critical (i.e. most integrally amplified) eigensolution reconcile with that of the most energetic unsteady perturbation observed in the DNS. In the subsequent nonlinear perturbation regime, DNS results show the interaction between two families of unsteady vortices shed from the shear layer surrounding the CS dip. The inception of these unsteady vortices spatially correlates with both the critical and subcritical instability eigenmodes. Overall, the present findings from secondary linear stability analysis and DNS support and expand key conclusions from recent experimental studies (Rius-Vidales & Kotsonis 2022), providing further evidence for the generality of the proposed model for unsteady effects driving transition at the step.

The CS dip is an inherent feature of the shear-layer deformation, whose origin shall be ascribed to the interaction between the step flow and the stationary content of incoming perturbations. From a structural viewpoint, the stationary perturbation field consists of the incoming CFI passing over the step and locally induced perturbation streaks at the upper step corner (Casacuberta *et al.* 2021, 2022*b*). To elucidate the mechanisms responsible for this stationary shear-layer deformation, energy-balance equations of the

https://doi.org/10.1017/jfm.2026.11854 Published online by Cambridge University Press

stationary spanwise-harmonic perturbation modes are formulated. The analysis reveals that the CS dip is the manifestation of a set of high-order spanwise perturbation modes that undergo spatial amplification at the step via two primary mechanisms, namely, (i) the linear destabilisation by an inflectional instability of the base-flow profiles downstream of the step, and (ii) the nonlinear effect associated with the interaction between spanwise perturbation modes. The former takes place in the region farther from the wall, i.e. dominated by the incoming CFI, whilst the latter develops very close to the wall, i.e. in the region dominated by the perturbation streaks generated at the upper step corner.

These insights are presently leveraged to propose that the step alters the transition route, relative to a no-step scenario, through a spatial non-modal growth effect. This non-modal growth effect, which manifests as locally formed near-wall streaks (Casacuberta *et al.* 2025) and is in turn pre-conditioned by the incoming primary (crossflow) instability, contributes to the steady deformation of the flow at the step supporting the growth of unsteady eigensolutions and the onset of turbulence.

Acknowledgements. The authors would like to express their gratitude to Dr Rius-Vidales and Dr Westerbeek for fruitful discussions. The authors also wish to honour the memory of Professor J.L. van Ingen (1932–2023), a foundational figure in the study of boundary-layer transition.

Funding. This work was performed on the Dutch national e-infrastructure with support from the SURF Cooperative under NWO grants no. 14078 and no. 15632. The authors acknowledge the support of the European Research Council through StG no. 803082 GLOWING and the Dutch Research Council through Vici grant no. 20647. Open access funding provided by Delft University of Technology.

Declaration of interests. The authors report no conflict of interest.

Appendix A. Details of the derivation of energy-balance equations of the stationary spanwise-harmonic perturbations

This appendix expands on the derivation of the energy-balance equation of the spanwise-harmonic perturbation modes presented in § 3.

Consider the non-dimensional form of the perturbation equation governing the evolution of a stationary perturbation field $\boldsymbol{q}' = [\boldsymbol{v}'\ p']^T$,

$$\left(\underline{\boldsymbol{v}}' \cdot \boldsymbol{\nabla}\right) \underline{\boldsymbol{v}}_B + \left(\underline{\boldsymbol{v}}_B \cdot \boldsymbol{\nabla}\right) \underline{\boldsymbol{v}}' = -\boldsymbol{\nabla} \underline{p}' + \frac{1}{Re} \boldsymbol{\nabla}^2 \underline{\boldsymbol{v}}' - \left(\underline{\boldsymbol{v}}' \cdot \boldsymbol{\nabla}\right) \underline{\boldsymbol{v}}', \tag{A1}$$

where the underline symbol indicates a non-dimensional quantity, with reference scales δ_0 and u_∞ (§ 2.1). For convenience, (A1) is rewritten as

$$0 = \mathcal{L}\left(\underline{\boldsymbol{v}}'\right) - \boldsymbol{\nabla} \underline{p}' - \left(\underline{\boldsymbol{v}}' \cdot \boldsymbol{\nabla}\right) \underline{\boldsymbol{v}}' \tag{A2}$$

by introducing the linear operator $\mathcal{L}(\underline{\boldsymbol{v}}') = -(\underline{\boldsymbol{v}}') \cdot \boldsymbol{\nabla} \underline{\boldsymbol{v}}_B - \underline{\boldsymbol{v}}_B \cdot \boldsymbol{\nabla}(\underline{\boldsymbol{v}}') + (1/Re)\boldsymbol{\nabla}^2(\underline{\boldsymbol{v}}')$.

The spanwise-harmonic decomposition of the stationary perturbation field (see (2.3) for $k = 0$) is inserted into (A2), which leads to

$$0 = \sum_{j=-N}^{N} \left(\mathcal{L}\left(\tilde{\underline{\boldsymbol{v}}}_{(0,j)}\, \mathrm{e}^{ij\beta_0 z}\right) - \boldsymbol{\nabla}\left(\tilde{\underline{p}}_{(0,j)}\, \mathrm{e}^{ij\beta_0 z}\right) - \left(\tilde{\underline{\boldsymbol{v}}}_{(0,j)}\, \mathrm{e}^{ij\beta_0 z}\right) \cdot \sum_{k=-N}^{N} \boldsymbol{\nabla}\left(\tilde{\underline{\boldsymbol{v}}}_{(0,k)}\, \mathrm{e}^{ik\beta_0 z}\right) \right). \tag{A3}$$

The terms of (A3) are re-expressed as

$$-\boldsymbol{\nabla}\left(\tilde{\underline{p}}_{(0,j)}\, \mathrm{e}^{ij\beta_0 z}\right) = -\boldsymbol{\nabla}\left(\tilde{\underline{p}}_{(0,j)}\right) \mathrm{e}^{ij\beta_0 z} - \mathrm{i}j\underline{\beta}_0 \tilde{\underline{p}}_{(0,j)}\, [0\,0\,1]^T\, \mathrm{e}^{ij\beta_0 z} = \mathbb{F}^p_{(0,j)}\, \mathrm{e}^{ij\beta_0 z}, \tag{A4}$$

https://doi.org/10.1017/jfm.2026.11854 Published online by Cambridge University Press

$$-\left(\tilde{\underline{\boldsymbol{v}}}_{(0,j)}\,\mathrm{e}^{ij\beta_0 z}\right)\cdot\nabla\underline{\boldsymbol{v}}_B=\mathbb{A}^{I}_{(0,j)}\,\mathrm{e}^{ij\beta_0 z},\tag{A5}$$

$$-\underline{\boldsymbol{v}}_B\cdot\nabla\left(\tilde{\underline{\boldsymbol{v}}}_{(0,j)}\,\mathrm{e}^{ij\beta_0 z}\right)=-\underline{\boldsymbol{v}}_B\cdot\left(\nabla(\mathrm{e}^{ij\beta_0 z})\otimes\tilde{\underline{\boldsymbol{v}}}_j+\nabla(\tilde{\underline{\boldsymbol{v}}}_j)\,\mathrm{e}^{ij\beta_0 z}\right)=\mathbb{A}^{II}_{(0,j)}\,\mathrm{e}^{ij\beta_0 z},\tag{A6}$$

$$\frac{1}{Re}\nabla^2\left(\tilde{\underline{\boldsymbol{v}}}_{(0,j)}\,\mathrm{e}^{ij\beta_0 z}\right)=\frac{1}{Re}\left(\tilde{\underline{\boldsymbol{v}}}_{(0,j)}\nabla^2(\mathrm{e}^{ij\beta_0 z})+2(\nabla(\mathrm{e}^{ij\beta_0 z})\cdot\nabla)\tilde{\underline{\boldsymbol{v}}}_{(0,j)}+\mathrm{e}^{ij\beta_0 z}\,\nabla^2\tilde{\underline{\boldsymbol{v}}}_{(0,j)}\right)=\mathbb{F}^{v}_{(0,j)}\,\mathrm{e}^{ij\beta_0 z}.\tag{A7}$$

The vector coefficients $\mathbb{A}^{I}_{(0,j)}(x,y)$, $\mathbb{A}^{II}_{(0,j)}(x,y)$, $\mathbb{F}^{v}_{(0,j)}(x,y)$, $\mathbb{F}^{p}_{(0,j)}(x,y)$, $-N\leqslant j\leqslant N$, read

$$\mathbb{A}^{I}_{(0,j)}=\begin{bmatrix}-\tilde{\underline{u}}_{(0,j)}\dfrac{\partial\underline{u}_B}{\partial\underline{x}}-\tilde{\underline{v}}_{(0,j)}\dfrac{\partial\underline{u}_B}{\partial\underline{y}}\\[2mm]-\tilde{\underline{u}}_{(0,j)}\dfrac{\partial\underline{v}_B}{\partial\underline{x}}-\tilde{\underline{v}}_{(0,j)}\dfrac{\partial\underline{v}_B}{\partial\underline{y}}\\[2mm]-\tilde{\underline{u}}_{(0,j)}\dfrac{\partial\underline{w}_B}{\partial\underline{x}}-\tilde{\underline{v}}_{(0,j)}\dfrac{\partial\underline{w}_B}{\partial\underline{y}}\end{bmatrix},\quad \mathbb{A}^{II}_{(0,j)}=\begin{bmatrix}-\underline{u}_B\dfrac{\partial\tilde{\underline{u}}_{(0,j)}}{\partial\underline{x}}-\underline{v}_B\dfrac{\partial\tilde{\underline{u}}_{(0,j)}}{\partial\underline{y}}-\mathrm{i}j\underline{\beta}_0\underline{w}_B\tilde{\underline{u}}_{(0,j)}\\[2mm]-\underline{u}_B\dfrac{\partial\tilde{\underline{v}}_{(0,j)}}{\partial\underline{x}}-\underline{v}_B\dfrac{\partial\tilde{\underline{v}}_{(0,j)}}{\partial\underline{y}}-\mathrm{i}j\underline{\beta}_0\underline{w}_B\tilde{\underline{v}}_{(0,j)}\\[2mm]-\underline{u}_B\dfrac{\partial\tilde{\underline{w}}_{(0,j)}}{\partial\underline{x}}-\underline{v}_B\dfrac{\partial\tilde{\underline{w}}_{(0,j)}}{\partial\underline{y}}-\mathrm{i}j\underline{\beta}_0\underline{w}_B\tilde{\underline{w}}_{(0,j)}\end{bmatrix},\tag{A8}$$

$$\mathbb{F}^{p}_{(0,j)}=\begin{bmatrix}-\dfrac{\partial\tilde{\underline{p}}_{(0,j)}}{\partial\underline{x}}\\[2mm]-\dfrac{\partial\tilde{\underline{p}}_{(0,j)}}{\partial\underline{y}}\\[2mm]-\mathrm{i}j\underline{\beta}_0\tilde{\underline{p}}_{(0,j)}\end{bmatrix},\qquad \mathbb{F}^{v}_{(0,j)}=\frac{1}{Re}\begin{bmatrix}-(j)^2\underline{\beta}_0^2\,\tilde{\underline{u}}_{(0,j)}+\dfrac{\partial^2\tilde{\underline{u}}_{(0,j)}}{\partial\underline{x}^2}+\dfrac{\partial^2\tilde{\underline{u}}_{(0,j)}}{\partial\underline{y}^2}\\[2mm]-(j)^2\underline{\beta}_0^2\,\tilde{\underline{v}}_{(0,j)}+\dfrac{\partial^2\tilde{\underline{v}}_{(0,j)}}{\partial\underline{x}^2}+\dfrac{\partial^2\tilde{\underline{v}}_{(0,j)}}{\partial\underline{y}^2}\\[2mm]-(j)^2\underline{\beta}_0^2\,\tilde{\underline{w}}_{(0,j)}+\dfrac{\partial^2\tilde{\underline{w}}_{(0,j)}}{\partial\underline{x}^2}+\dfrac{\partial^2\tilde{\underline{w}}_{(0,j)}}{\partial\underline{y}^2}\end{bmatrix}.\tag{A9}$$

Finally, the nonlinear term is expanded as

$$\begin{aligned}-\tilde{\underline{\boldsymbol{v}}}_{(0,j)}\,\mathrm{e}^{ij\beta_0 z}\cdot\sum_{k=-N}^{N}\nabla\left(\tilde{\underline{\boldsymbol{v}}}_{(0,k)}\,\mathrm{e}^{ik\beta_0 z}\right)&=-\tilde{\underline{\boldsymbol{v}}}_{(0,j)}\,\mathrm{e}^{ij\beta_0 z}\cdot\sum_{k=-N}^{N}\left(\nabla(\mathrm{e}^{ik\beta_0 z})\otimes\tilde{\underline{\boldsymbol{v}}}_{(0,k)}+\nabla(\tilde{\underline{\boldsymbol{v}}}_k)\mathrm{e}^{ik\beta_0 z}\right)\\&=-\tilde{\underline{\boldsymbol{v}}}_{(0,j)}\,\mathrm{e}^{ij\beta_0 z}\cdot\sum_{k=-N}^{N}\left(\mathbb{B}_{(0,k)}\,\mathrm{e}^{ik\beta_0 z}\right)=-\mathrm{e}^{ij\beta_0 z}\sum_{\substack{r=-N\\ j-r\in[-N,N]}}^{N}\left(\tilde{\underline{\boldsymbol{v}}}_{(0,r)}\cdot\mathbb{B}_{(0,j-r)}\right),\end{aligned}\tag{A10}$$

where both indices r and $j-r$ lie within the truncated mode range $[-N,N]$ and

$$\mathbb{B}_{(0,k)}=\begin{bmatrix}\dfrac{\partial\tilde{\underline{u}}_k}{\partial\underline{x}}&\dfrac{\partial\tilde{\underline{v}}_k}{\partial\underline{x}}&\dfrac{\partial\tilde{\underline{w}}_k}{\partial\underline{x}}\\[2mm]\dfrac{\partial\tilde{\underline{u}}_k}{\partial\underline{y}}&\dfrac{\partial\tilde{\underline{v}}_k}{\partial\underline{y}}&\dfrac{\partial\tilde{\underline{w}}_k}{\partial\underline{y}}\\[2mm]\mathrm{i}k\underline{\beta}_0\tilde{\underline{u}}_k&\mathrm{i}k\underline{\beta}_0\tilde{\underline{v}}_k&\mathrm{i}k\underline{\beta}_0\tilde{\underline{w}}_k\end{bmatrix},\tag{A11}$$

https://doi.org/10.1017/jfm.2026.11854 Published online by Cambridge University Press

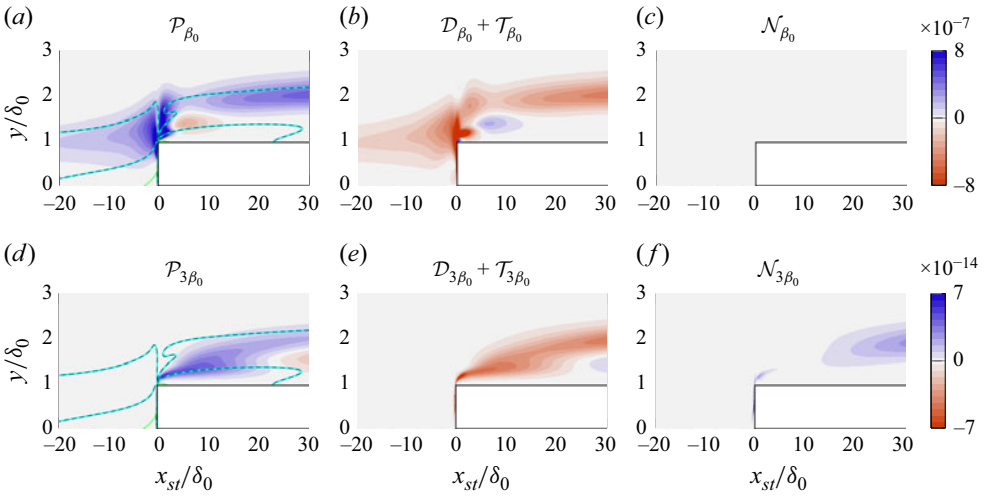


Figure 26. Spatial evolution of budget terms of (3.4) in case s.*A* for $n=1$ (top) and $n=3$ (bottom): (*a*,*d*) energy production, (*b*,*e*) viscous effects and energy advection, (*c*,*f*) work of nonlinear interactions. Loci of crossflow inflection points in the base flow (solid cyan line) and by the addition of the mean-flow distortion (dashed black line) and base-flow reversal $u_B=0$ (dotted green line) in (*a*, *d*).

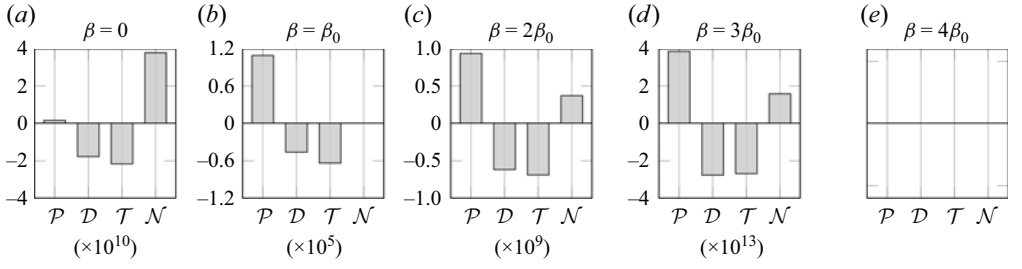


Figure 27. Integral contribution over S of budget terms in (3.4) for case s.*A* shown for $n=0$ (*a*), 1 (*b*), 2 (*c*), 3 (*d*). Subplot (*e*) is intentionally left empty due to precision constraints.

with the index $j-r$ in (A10) being denoted by k.

Appendix B

This appendix provides additional quantification of energy budgets derived from the balance equations presented in § 3 and Appendix A and discussed in § 5. First, figures 26 and 27 present the energy-budget analysis of § 5 applied to case s.*A*. Figure 26 illustrates the spatial evolution of budget terms, while figure 27 quantifies their integral evaluation over the surface S, following the same methodology used for cases s.*B* and s.*C* in § 5.

Appendix C

This appendix compares the evolution of the critical (i.e. most integrally amplified) unsteady stability eigenmode, CS-mode$_1$ at $f=12$ kHz (§ 6.2), between the plane-marching (blue dashed lines) and local (red dotted) stability approaches and the DNS (solid black) in figure 28.

https://doi.org/10.1017/jfm.2026.11854 Published online by Cambridge University Press

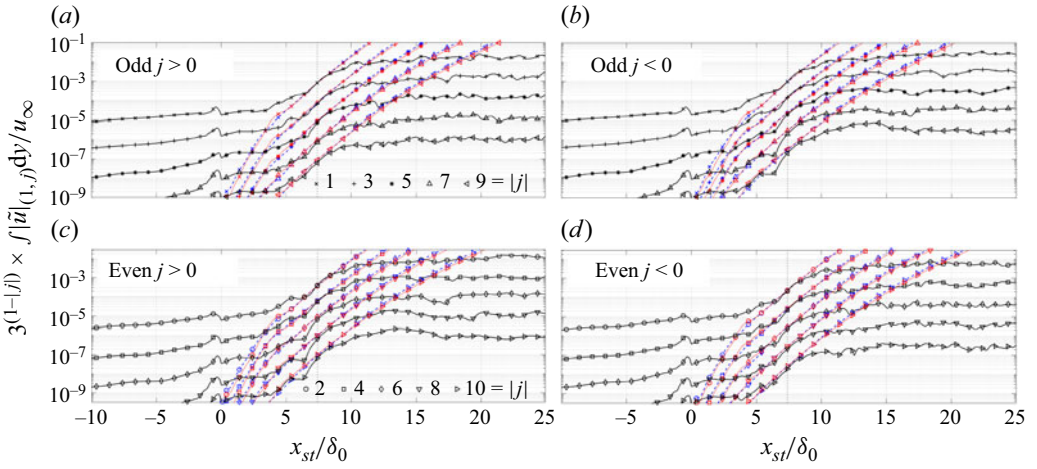


Figure 28. Perturbation amplitudes for the odd (a, b) and even (c, d) z-Fourier harmonics $|\tilde{u}|_{(12,j)}$ at 12 kHz attributed to CS-mode$_1$ as computed with plane marching (blue dashed lines) and local (red dotted lines) stability approaches and DNS (solid black lines). Amplitudes of the linear approaches' $|\tilde{u}|_{(12,1)}$ harmonics (crosses in panel a) are matched to the DNS equivalent at $x_{st}/\delta_0 = 7.39$ (vertical dashed line). Note that amplitude values are scaled by negative powers of 3 for ease of visualisation.

Appendix D

This appendix provides confidence that the presently considered step flow is convectively unstable only. To this end, a test is carried out for absolute instability (Huerre & Monkewitz 1985). As described by Koch *et al.* (2000, p. 135), within the scope of classic secondary CFI modes, absolute instability requires the satisfaction of the following two conditions.

(i) The modal-coincidence condition: a double α_θ eigenvalue occurs at a frequency with positive imaginary part ($\omega_i > 0$); this solution's group speed equals zero, $c_g = 0$.
(ii) The pinching condition: as $\omega_i \to +\infty$, one $\alpha_{\theta,i} \to +\infty$, while the other $\alpha_{\theta,i} \to -\infty$. Observing this condition, the numerator of the last equation in (6.3) for c_g dictates that the former and latter α_θ solutions have positive and negative group speeds in the limit, respectively; see Briggs (1964 p. 20).

Two instances of a double α_θ eigenvalue are presented in table 5. They are found by repeatedly solving the temporal problem (that is, solving the local problem for ω given α_θ), while inputting the average of two close α_θ eigenvalues and the spatial problem (that is, solving for α_θ given ω) while inputting the ω eigenvalue that varies the least. This was done at (the arbitrary) x locations were $\alpha_{\theta,i}$ as graphed versus x and real f appeared to display a branch point; double α_θ eigenvalues can be traced to other x locations. For the considered x location, it is found that the pinching condition is not satisfied. However, figure 29 shows that $\alpha_{\theta,i} \to +\infty$ for all considered eigenmodes. Hence, even if $\omega_i > 0$ marginally for the coincidence between CS modes 1 and 2, the presently considered CS modes do not constitute an absolute instability mechanism. Besides the comparison in figure 20, the demonstration that the flow is not absolutely unstable (which also implies being globally stable; see Huerre & Monkewitz 1990; Monkewitz *et al.* 1993) strengthens our confidence that the perturbations can be accurately modelled with a plane-marching approach downstream of the step, even if this region supports reverse flow.

https://doi.org/10.1017/jfm.2026.11854 Published online by Cambridge University Press

CS modes	f (Hz)	x_{st}/δ_0	θ (°)	$-\alpha_{\theta,i}\delta_0$	$\alpha_{\theta,r}\delta_0$	$\lvert\Delta\alpha_\theta\rvert\delta_0$
2−3	12148 − 76.20i	2.685	−40.7	1.020	5.102	3.03×10^{-7}
1−2	7405 + 6.226i	1.085	−54.6	1.035	2.360	1.33×10^{-6}

Table 5. The CS-mode characteristics for frequencies that result in a double α_θ eigenvalue as computed with the local approach. Here $\Delta\alpha_\theta$ is the distance between the α_θ eigenvalues after converging the value of $\omega = 2\pi f$ to machine precision ($\Delta\omega/\Delta\alpha_\theta \sim c_g \to 0$ implies a relatively large uncertainty in α_θ vs ω).

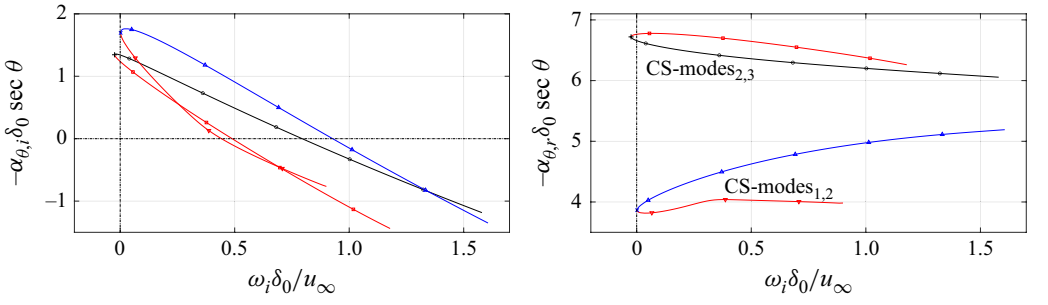


Figure 29. Loci of $\alpha_{\theta,i}$ and $\alpha_{\theta,r}$ as ω_i is varied from the value corresponding to the double α_θ eigenvalues (cross and plus symbols) to infinity. All considered $\alpha_{\theta,i} \to +\infty$, hence, the pinching condition is not satisfied (Briggs 1964).

References

Åkervik, E., Brandt, L., Henningson, D.S., Hoepffner, J., Marxen, O. & Schlatter, P. 2006 Steady solutions of the Navier–Stokes equations by selective frequency damping. *Phys. Fluids* **18**, 068102.

Ambrosino, B., Tocci, F., Theiss, A., Hein, S. & Rodríguez, D. 2025 Stationary crossflow vortices' secondary instability: linear stability theory and parabolized stability equations. *AIAA J.* **63** (6), 2182–2198.

Andersson, P., Brandt, L., Bottaro, A. & Henningson, D.S. 2001 On the breakdown of boundary layer streaks. *J. Fluid Mech.* **428**, 29–60.

Andersson, P., Henningson, D.S. & Hanifi, A. 1998 On a stabilization procedure for the parabolic stability equations. *J. Engng Maths* **33**, 311–332.

Arnal, D. 1993 Boundary layer transition: predictions based on linear theory. *Tech. Rep.* AGARD R-793. Advisory Group for Aerospace Research & Development (AGARD).

Asai, M., Minagawa, M. & Nishioka, M. 2002 The instability and breakdown of a near-wall low-speed streak. *J. Fluid Mech.* **455**, 289–314.

Bippes, H. 1999 Basic experiments on transition in the three-dimensional boundary layers dominated by crossflow instability. *Prog. Aerosp. Sci.* **35**, 363–412.

Bonfigli, G. & Kloker, M. 2007 Secondary instability of crossflow vortices: validation of the stability theory by direct numerical simulation. *J. Fluid Mech.* **583**, 229–272.

Brandt, L. 2007 Numerical studies of the instability and breakdown of a boundary-layer low-speed streak. *Eur. J. Mech. B Fluids* **26**, 64–82.

Brandt, L., Cossu, C., Chomaz, J.-M., Huerre, P. & Henningson, D.S. 2003 On the convectively unstable nature of optimal streaks in boundary layers. *J. Fluid Mech.* **485**, 221–242.

Brandt, L. & Henningson, D.S. 2002 Transition of streamwise streaks in zero-pressure-gradient boundary layers. *J. Fluid Mech.* **472**, 229–261.

Brandt, L., Schlatter, P. & Henningson, D.S. 2004 Transition in boundary layers subject to free-stream turbulence. *J. Fluid Mech.* **517**, 167–198.

Breuer, K.S. & Kuraishi, T. 1994 Transient growth in two- and three-dimensional boundary layers. *Phys. Fluids* **6**, 1983–1993.

Briggs, R.J. 1964 *Electron-Stream Interaction with Plasmas*. MIT Press.

Butler, K.M. & Farrell, B.F. 1992 Three-dimensional optimal perturbations in viscous shear flow. *Phys. Fluids A* **14**, 1426–1441.

https://doi.org/10.1017/jfm.2026.11854 Published online by Cambridge University Press

CASACUBERTA, J., GROOT, K.J., HICKEL, S. & KOTSONIS, M. 2022a Secondary instabilities in swept-wing boundary layers: direct numerical simulations and biglobal stability analysis. In *AIAA Paper* 2022-2330.

CASACUBERTA, J., GROOT, K.J., HICKEL, S. & KOTSONIS, M. 2023 How do forward-facing steps promote laminar-turbulent transition of swept-wing flow? In *Proceedings of the 14th International ERCOFTAC Symposium on Engineering Turbulence Modelling and Measurements*.

CASACUBERTA, J., GROOT, K.J., TOL, H.J. & HICKEL, S. 2018 Effectivity and efficiency of selective frequency damping for the computation of unstable steady-state solutions. *J. Comput. Phys.* **375**, 481–497.

CASACUBERTA, J., GROOT, K.J., YE, Q. & HICKEL, S. 2020 Transitional flow dynamics behind a micro-ramp. *Flow Turbul. Combust.* **104**, 533–552.

CASACUBERTA, J., HICKEL, S. & KOTSONIS, M. 2021 Mechanisms of interaction between stationary crossflow instabilities and forward-facing steps. In *AIAA Paper* 2021-0854.

CASACUBERTA, J., HICKEL, S. & KOTSONIS, M. 2024 Passive stabilization of crossflow instabilities by a reverse lift-up effect. *Phys. Rev. Fluid* **9**, 043903.

CASACUBERTA, J., HICKEL, S., WESTERBEEK, S. & KOTSONIS, M. 2022*b* Direct numerical simulation of interaction between a stationary crossflow instability and forward-facing steps. *J. Fluid Mech.* **943**, A46.

CASACUBERTA, J., WESTERBEEK, S., SUMARIVA, J.A.F., GROOT, K.J., HICKEL, S., HEIN, S. & KOTSONIS, M. 2025 Streaky perturbations in swept-wing flow over forward-facing step. *Phys. Rev. Fluid* **10**, 023902.

CHOUDHARI, M., LI, F., PAREDES, P. & DURAN, L. 2022 Evolution of high-frequency instabilities in the presence of azimuthally compact crossflow vortex pattern over a yawed cone. *Theor. Comput. Fluid Dyn.* **36**, 181–204.

CORBETT, P. & BOTTARO, A. 2001 Optimal linear growth in swept boundary layers. *J. Fluid Mech.* **435**, 1–23.

CROUCH, J.D. 2022 Predicting laminar-turbulent transition influenced by surface-induced flow distortions. In *IUTAM Symposium on Laminar-Turbulent Transition: 9th IUTAM Symposium, London, UK, September 2–6, 2019* (ed. S. Sherwin, P. Schmid & X. Wu), pp. 19–32. Springer.

DE TULLIO, N., PAREDES, P., SANDHAM, N.D. & THEOFILIS, V. 2013 Laminar-turbulent transition induced by a discrete roughness element in a supersonic boundary layer. *J. Fluid Mech.* **735**, 613–646.

DEYHLE, H. & BIPPES, H. 1996 Disturbance growth in an unstable three-dimensional boundary layer and its dependence on environmental conditions. *J. Fluid Mech.* **316**, 73–113.

DRAKE, A., BENDER, A., KORNTHEUER, A., WESTPHAL, R.V., MCKEON, B.J., GERASHCHENKO, S., ROHE, W. & DALE, G. 2010 Step excrescence effects for manufacturing tolerances on laminar flow wings. In *AIAA Paper* 2010-375.

DUNCAN, G.T.Jr., CRAWFORD, B.K., TUFTS, M.W., SARIC, W.S. & REED, H.L. 2013 Effects of step excrescences on swept-wing transition. In *AIAA Paper* 2013-2412.

ELLINGSEN, T. & PALM, E. 1975 Stability of linear flow. *Phys. Rev. Fluid* **18**, 487–488.

EPPINK, J.L. 2020 Mechanisms of stationary cross-flow instability growth and breakdown induced by forward-facing steps. *J. Fluid Mech.* **897**, A15.

FISCHER, T.M. & DALLMANN, U. 1991 Primary and secondary stability analysis of a three-dimensional boundary-layer flow. *Phys. Fluids A: Fluid Dyn.* **3** (10), 2378–2391.

GROOT, K.J., CASACUBERTA, J. & HICKEL, S. 2025 Non-orthogonal plane-marching stability equations for the secondary instability of crossflow vortices. *J. Comput. Phys.* **306**, 106947.

GROOT, K.J., SERPIERI, J., PINNA, F. & KOTSONIS, M. 2018 Secondary crossflow instability through global analysis of measured base flows. *J. Fluid Mech.* **846**, 605–653.

HAYNES, T.S. & REED, H.L. 2000 Simulation of swept-wing vortices using nonlinear parabolized stability equations. *J. Fluid Mech.* **405**, 325–349.

HÖGBERG, M. & HENNINGSON, D. 1998 Secondary instability of cross-flow vortices in Falkner–Skan–Cooke boundary layers. *J. Fluid Mech.* **368**, 339–357.

HUERRE, P. & MONKEWITZ, P.A. 1985 Absolute and convective instabilities in free shear layers. *J. Fluid Mech.* **159**, 151–168.

HUERRE, P. & MONKEWITZ, P.A. 1990 Local and global instabilities in spatially developing flows. *Annu. Rev. Fluid Mech.* **22** (1), 473–537.

HUNT, J., WRAY, A. & MOIN, P. 1988 *Eddies, streams, and convergence zones in turbulent flows*. Report CTR-S88. Center for Turbulence Research.

JACOBS, R.G. & DURBIN, P.A. 2001 Simulations of bypass transition. *J. Fluid Mech.* **482**, 185–212.

JIN, B., SYMON, S. & ILLINGWORTH, S.J. 2021 Energy transfer mechanisms and resolvent analysis in the cylinder wake. *Phys. Rev. Fluid* **6**, 024702.

KENDALL, J.M. 1985 Experimental study of disturbances produced in a pre-transitional laminar boundary layer by weak free-stream turbulence. *AIAA Pap.* **85**, 1695.

https://doi.org/10.1017/jfm.2026.11854 Published online by Cambridge University Press

KLEBANOFF, P.S. 1971 Effect of free-stream turbulence on the laminar boundary layer. *Bull. Am. Phys. Soc.* **10**, 1305–1323.
KOCH, W., BERTOLLOTI, F.P., STOLTE, A. & HEIN, S. 2000 Nonlinear equilibrium solutions in a three-dimensional boundary layer and their secondary instability. *J. Fluid Mech.* **406**, 131–174.
KONISHI, Y. & ASAI, M. 2004 Experimental investigation of the instability of spanwise-periodic low-speed streaks. *Fluid Dyn. Res.* **34**, 299–315.
KURZ, H.B.E. & KLOKER, M.J. 2016 Mechanisms of flow tripping by discrete roughness elements in a swept-wing boundary layer. *J. Fluid Mech.* **796**, 158–194.
LANDAHL, M.T. 1975 Wave breakdown and turbulence. *SIAM J. Appl. Math.* **28**, 735–756.
LANDAHL, M.T. 1980 A note on an algebraic instability of inviscid parallel shear flows. *J. Fluid Mech.* **98**, 243–251.
LANZERSTORFER, D. & KUHLMANN, H.C. 2012 Three-dimensional instability of the flow over a forward-facing step. *J. Fluid Mech.* **695**, 390–404.
LI, F., CHOUDHARI, M., PAREDES, P. & DUAN, L. 2016*a* High-frequency instabilities of stationary crossflow vortices in a hypersonic boundary layer. *Phys. Rev. Fluid* **1**, 053603.
LI, F. & CHOUDHARI, M.M. 2011 Spatially developing secondary instabilities in compressible swept airfoil boundary layers. *Theor. Comput. Fluid Dyn.* **25**, 65–84.
LI, F., CHOUDHARI, M.M. & DUAN, L. 2016*b* Stationary crossflow breakdown due to mixed mode spectra of secondary instabilities. In *AIAA Paper* 2016-3789.
LOISEAU, J.-C., ROBINET, J.-C., CHERUBINI, S. & LERICHE, E. 2014 Investigation of the roughness-induced transition: global stability analyses and direct numerical simulations. *J. Fluid Mech.* **760**, 175–211.
MACK, L. 1984 *Boundary layer linear stability theory*. *Tech. Rep.* AGARD No. 709. Advisory Group for Aerospace Research & Development (AGARD).
MALIK, M.R., LI, F., CHOUDHARI, M.M. & CHANG, C.-L. 1999 Secondary instability of crossflow vortices and swept-wing boundary-layer transition. *J. Fluid Mech.* **399**, 85–115.
MARINO, L. & LUCHINI, P. 2009 Adjoint analysis of the flow over a forward-facing step. *Theor. Comput. Fluid Dyn.* **23**, 37–54.
MATSUBARA, M. & ALFREDSSON, P.H. 2001 Disturbance growth in boundary layers subjected to free-stream turbulence. *J. Fluid Mech.* **430**, 149–168.
MONKEWITZ, P.A., HUERRE, P. & CHOMAZ, J.-M. 1993 Global linear stability analysis of weakly non-parallel shear flows. *J. Fluid Mech.* **251**, 1–20.
MORKOVIN, M.V. 1969 *On the Many Faces of Transition*. Springer.
MORKOVIN, M.V., RESHOTKO, E. & HERBERT, T. 1994 Transition in open flow systems–a reassessment. *Bull. Am. Phys. Soc.* **39**, 1882.
PAREDES, P. 2014 Advances in global instability computations: from incompressible to hypersonic flow. PhD Dissertation, Universidad Politécnica De Madrid.
PAREDES, P., HANIFI, A., THEOFILIS, V. & HENNINGSON, D.S. 2015 The nonlinear PSE-3D concept for transition prediction in flows with a single slowly-varying spatial direction. *Procedia IUTAM* **14**, 36–44.
REDDY, S.C. & HENNINGSON, D.S. 1993 Energy growth in viscous channel flows. *J. Fluid Mech.* **252**, 209–238.
RESHOTKO, E. 2001 Transient growth: a factor in bypass transition. *Phys. Fluids* **13**, 1067–1075.
RICCO, P., LUO, J. & WU, X. 2011 Evolution and instability of unsteady nonlinear streaks generated by free-stream vortical disturbances. *J. Fluid Mech.* **677**, 1–38.
RIUS-VIDALES, A.F. & KOTSONIS, M. 2020 Influence of a forward-facing step surface irregularity on swept wing transition. *AIAA J.* **58** (12), 5243–5253.
RIUS-VIDALES, A.F. & KOTSONIS, M. 2021 Impact of a forward-facing step on the development of crossflow instability. *J. Fluid Mech.* **924**, A34.
RIUS-VIDALES, A.F. & KOTSONIS, M. 2022 Unsteady interaction of crossflow instability with a forward-facing step. *J. Fluid Mech.* **939**, A19.
SARIC, W.S., REED, H.L. & WHITE, E.B. 2003 Stability and transition of three-dimensional boundary layers. *Annu. Rev. Fluid Mech.* **35**, 413–440.
SCHMID, P.J. & HENNINGSON, D.S. 2001 *Stability and Transition in Shear Flows*. Springer.
SERPIERI, J. & KOTSONIS, M. 2016 Three-dimensional organisation of primary and secondary crossflow instability. *J. Fluid Mech.* **799**, 200–245.
SMITH, A.M.O. & CLUTTER, D.W. 1959 The smallest height of roughness capable of affecting boundary-layer transition. *J. Aerosp. Sci.* **26** (4), 229–245.
SOMBAERT, L., *et al.* 2025 Ground tests on BOLT at Mach 7: cross-facility comparison and stability analysis. *AIAA J.* **63** (6), 2135–2150.

https://doi.org/10.1017/jfm.2026.11854 Published online by Cambridge University Press

STÜER, H., GYR, A. & KINZELBACH, W. 1999 Laminar separation on a forward facing step. *Eur. J. Mech. B Fluids* **18**, 675–692.

SWEARINGEN, J.D. & BLACKWELDER, R.F. 1987 The growth and breakdown of streamwise vortices in the presence of a wall. *J. Fluid Mech.* **182**, 255–290.

TEMPELMANN, D., HANIFI, A. & HENNINGSON, D.S. 2010 Spatial optimal growth in three-dimensional boundary layers. *J. Fluid Mech.* **646**, 5–37.

THEOFILIS, V. 2003 Advances in global linear instability analysis of nonparallel and three-dimensional flows. *Prog. Aerosp. Sci.* **39**, 249–315.

TREFETHEN, L.N., TREFETHEN, A.E., REDDY, S.C. & DRISCOLL, T.A. 1993 Hydrodynamic stability without eigenvalues. *Science* **28**, 578–584.

TUFTS, M.W., REED, H.L., CRAWFORD, B.K., G.T. DUNCAN Jr., SARIC, W.S. 2017 Computational investigation of step excrescence sensitivity in a swept-wing boundary layer. *J. Aircraft* **54**, 602–626.

WASSERMANN, P. & KLOKER, M. 2002 Mechanisms and passive control of crossflow-vortex-induced transition in a three-dimensional boundary layer. *J. Fluid Mech.* **456**, 49–84.

WASSERMANN, P. & KLOKER, M. 2005 Transition mechanisms in a three-dimensional boundary-layer flow with pressure-gradient changeover. *J. Fluid Mech.* **530**, 265–293.

WEI, H., TENDERO, J.A., PAREDES, P. & THEOFILIS, V. 2017 Linear instability in the wake of an elliptic wing. *Theor. Comput. Fluid Dyn.* **31**, 483–504.

WESTIN, A.K.J., BOIKO, A.V., KLINGMANN, B.G.B., KOZLOV, V.V. & ALFREDSSON, P.H. 1994 Experiments in a boundary layer subjected to free stream turbulence. Part 1. Boundary layer structure and receptivity. *J. Fluid Mech.* **281**, 193–218.

WHITE, E.B. & SARIC, W.S. 2005 Secondary instability of crossflow vortices. *J. Fluid Mech.* **525**, 275–308.

WILHELM, D., HÄRTEL, C. & KLEISER, L. 2003 Computational analysis of the two-dimensional-three-dimensional transition in forward-facing step flow. *J. Fluid Mech.* **489**, 1–27.

ZAKI, T.A. & DURBIN, P.A. 2005 Mode interaction and the bypass route to transition. *J. Fluid Mech.* **531**, 85–111.

https://doi.org/10.1017/jfm.2026.11854 Published online by Cambridge University Press